

1 JUICE-MAJIS Earth observations during the 2024 gravity assist: first analysis 2 and comparison with PRISMA data

3

4 Fabrizio Oliva^{1,*}, Emiliano D'Aversa¹, Alessandra Migliorini², Giuseppe Piccioni¹, François Poulet³;
5 Yves Langevin³, Gianrico Filacchione¹, Mauro Ciarniello¹, Sébastien Rodriguez³, Benoît Seignovert⁵,
6 Alessandro Mura¹, Leigh N. Fletcher⁴, Sandrine Guerlet^{6,7}, Angelo Zinzi⁸, Marco Giardino⁸, Ettore
7 Lopinto⁸, Giuseppe Sindoni⁸, Christina Plainaki¹

8 *Correspondence: fabrizio.oliva@inaf.it

9

10 ¹Istituto di Astrofisica e Planetologia Spaziali (IAPS/INAF), Rome, Italy;

11 ²Osservatorio Astronomico di Padova (OAPd/INAF), Padova, Italy;

12 ³Institut d'Astrophysique Spatiale, CNRS/Université Paris-Saclay, 91405 Orsay Cedex, France;

13 ⁴School of Physics and Astronomy, University of Leicester, University Road, Leicester, LE1 7RH, UK;

14 ⁵OSUNA, UAR-3281, LPG UMR-6112, CNRS, Nantes Université, Nantes, France;

15 ⁶Laboratoire de Meteorologie Dynamique, LMD-IPSL, CNRS, Sorbonne Université, Université PSL,
16 Institut Polytechnique, Paris, France;

17 ⁷LIRA, Observatoire de Paris, Université PSL, CNRS, Sorbonne Université, Université Paris Cité,
18 92195 Meudon Cedex, France;

19 ⁸Agenzia Spaziale Italiana (ASI), Rome, Italy.

20

21 Abstract

22

23 The *JUpiter ICy moons Explorer* spacecraft (JUICE) performed a Lunar-Earth gravity assist
24 maneuver on 20th August 2024, during which the scientific instruments were turned on to
25 test their functionality. In the time of the Earth flyby, the *Moon and Jupiter Imaging*
26 *Spectrometer* (MAJIS) on board JUICE acquired a sequence of multispectral images over
27 the Western Pacific Ocean at tropical latitudes. In parallel, an observing campaign was also
28 conducted by the Earth-orbiting PRISMA imaging spectrometer, with the purpose of
29 validating MAJIS spectral observations with independent measurements of the same kind.

30 These two datasets are here exploited to investigate and compare several atmospheric and
31 cloud properties, including composition, temperatures, and atmospheric gravity waves. In the
32 MAJIS spectral range, covering the 500-5560 nm wavelengths, we identified major and
33 minor atmospheric gases, including O₂, H₂O, CO₂, O₃, CH₄, N₂O. Since MAJIS observations
34 mostly covered diffuse cloudiness over the ocean, our analysis mainly focused on the
35 discrimination of clouds' features and altitudes. We verified that ice particles are widespread
36 in the data, allowing for an investigation of their properties (e.g. crystallinity) through different
37 spectral signatures. The only land features identified in MAJIS data are not observed in
38 daylight, hence only a thermal emission analysis is presented. Finally, the coverage of the
39 4300 nm CO₂ band enables the identification of high altitude structures, revealing the
40 presence of several atmospheric wave packets, likely induced by convective events, or
41 lightning strikes known to have occurred at the time of the flyby. The present analysis
42 demonstrates how MAJIS data can contribute to the scientific investigation of an
43 atmospheric environment, and provide the first benchmark in the analysis of water ice,
44 whose characterization in the Jovian system will be of primary importance for the JUICE
45 mission.

46

47 1. Introduction

48

49 The JUICE mission is conceived for the investigation of Jupiter's icy satellites' surfaces and
50 interiors, but also for the characterization of the giant planet's atmosphere and
51 magnetosphere. These scientific objectives will be achieved thanks to a payload consisting
52 of several remote sensing and in-situ instruments, including an altimeter, a magnetometer, a
53 gravity experiment, a radio instrument, neutral/energetic particles and plasma detectors and
54 an ultraviolet spectrograph. Moreover, the visible-thermal infrared spectral range will be
55 investigated by a visible camera (JANUS) and by the *Moons and Jupiter Imaging*
56 *Spectrometer* (MAJIS, Poulet et al., 2024a), which in particular will allow the spectroscopic
57 investigation of Jupiter's atmosphere, moons and rings system.

58 On the 20th of August 2024 the JUICE spacecraft performed a *Lunar-Earth Gravity Assist*
59 (LEGA) and is now headed for a second *Earth Gravity Assist* (EGA) happening in September
60 2026. In this study we will focus on 2024 EGA data acquired by MAJIS which, along with
61 JANUS (see Hueso et al., this issue), was turned on providing its very first observations of a
62 planetary target (for a general overview of the flyby refer to Poulet et al., this issue, while
63 valuable information about MAJIS operations, functioning and performances is given in
64 Langevin et al. and Seignovert et al., this issue). During the flyby, different Earth observing
65 spectrometers were coordinated to provide spatially and temporally comparable
66 observations (Poulet et al., this issue). A companion paper by Guerlet et al. (this issue) is
67 focused on MAJIS IR channel's data comparison with co-located acquisitions by the IASI
68 thermal Fourier spectrometer onboard the EUMETSAT/Metop satellite. Instead, we exploit
69 PRISMA spectrometer data as a proxy to compare with MAJIS VISNIR channel observations
70 (Section 2.1), even if the different times and regions of acquisition prevent a direct
71 comparison of the scans (see Section 2). PRISMA (Section 2.2) is a technology
72 demonstrator mission completely funded by the Italian Space Agency (ASI) and devoted to
73 the qualification of a panchromatic/hyperspectral technology for monitoring the Earth at
74 visual-near infrared wavelengths at moderate spectral resolution and high spatial resolution
75 (Pignatti et al., 2013).

76 During the EGA, JUICE flew over Western Pacific Ocean at tropical latitudes, moving
77 approximately from Sumatra to Hawaii islands and spanning local times from about 03:00
78 10:30 (see Table 1). The majority of these measurements took place over the ocean,
79 allowing a broad characterization of atmospheric gaseous composition and structure
80 (Section 2.3.2). Land features are only marginally detected in a couple of observations
81 mainly in the thermal range (Section 4.4).

82 Given the widespread presence of clouds and the early local times of acquisition (Section 2),
83 ice is observed in almost all MAJIS scans (Section 4.1), allowing benchmarking of the
84 spectrometer's response to this observable in view of Jupiter's icy satellites investigation.
85 Also atmospheric waves, whose role is fundamental in regulating the middle-atmosphere
86 circulation (e.g. Hamilton, 1996; Fritts and Alexander, 2003), are detected in many MAJIS
87 observations. Such phenomena are either linked with orography (Queney 1948; Kim et al.
88 2003) or with the occurrence of thunderstorms (Taylor and Hapgood, 1988; Dewan et al.
89 1998). Given that MAJIS EGA observations mainly targeted the ocean, we investigate the
90 waves' connection with strong convective events or lightning strikes (Section 4.4).

91 The manuscript is arranged in sections describing the data (Section 2), the methods for their
92 investigation (Section 3) and the obtained results (Section 4). Such a wide ensemble of

93 atmospheric observable features is finally discussed in the context of Jupiter science in
94 Section 5.

95

96 2. Observations

97

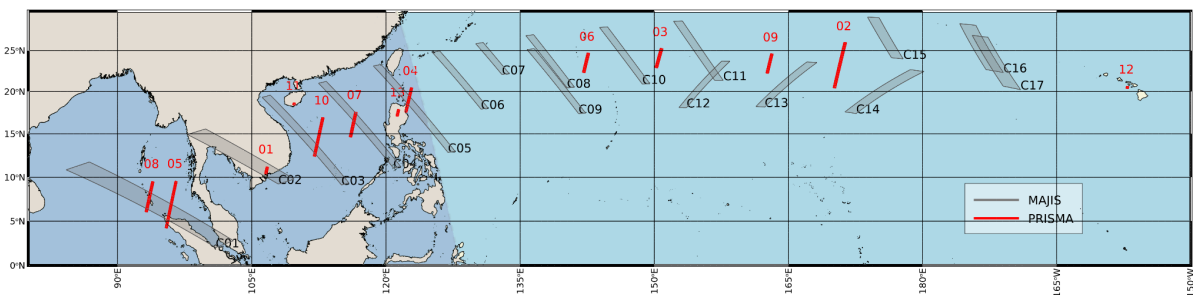
98 2.1. MAJIS EGA Data

99

100 MAJIS is a dispersion grating imaging spectrometer operating between 500 and 5560 nm by
101 means of two spectral channels (Poulet et al., 2024a). The first channel (VISNIR, 500–2350
102 nm) is characterized by nominal spectral resolution and sampling of 2.9-4.6 nm and 3.5-3.8
103 nm/band respectively, while the second (IR, 2270–5560 nm) works with a spectral resolution
104 of 5.5-7.0 nm and a sampling of 5.9-6.9 nm/band. The nominal instrument’s instantaneous
105 field of view (IFOV) is 150 μ rad/pixel. MAJIS concept has been optimized for the
106 characterization of the surface and near-surface environment of Jupiter’s icy moons (Poulet
107 et al., 2024a), as well as for the investigation of Jupiter’s atmosphere (Fletcher et al., 2023).
108 Detailed descriptions of the instrument functioning, operations and calibration are given in
109 Haffoud et al. (2024), Langevin et al. (2024), Poulet et al. (2024b), Filacchione et al. (2024),
110 Rodriguez et al. (2024), Vincendon et al. (2024), and Stefani et al.(2025). Scene geometry is
111 reconstructed via the SPICE-NAIF toolkit (Acton, 1996; Acton et al., 2018) and kernels
112 provided by ESA (“JUICE SPICE Kernel Dataset,” 2019).

113 Figure 1 and Table 1 summarize footprint locations and main basic properties of the 17
114 MAJIS EGA data investigated in this work (see Poulet et al., this issue, for further
115 instrumental parameters). Two additional cubes, targeted off-limb for calibration purposes
116 (Poulet et al., this issue), are not considered here. Each MAJIS acquisition consists of
117 hyperspectral *cubes* (i.e. 2D spatial frames with a third spectral dimension) collected as
118 pushbroom spectral scans via internal mirror rotation, with different widths and lengths.

119



120

121 **Figure 1:** Geographical coverage of the investigated observations, MAJIS in grey color,
122 PRISMA in red color. The darker area westward of the Philippines indicates the nightside at
123 the time of the terminator crossing of MAJIS observations (2024-Aug-20 21:30 UTC). Instead
124 all PRISMA footprints are in daylight, at local time ~10:30. Coastlines are from
125 OpenStreetMap, available under the Open Database License.

126

127 The first 4 cubes (C1 to C4) pointed to the Earth surface at nighttime and contain a
128 significant signal only in the thermal part of the spectrum ($\lambda > 3000$ nm). The only exception
129 is C1, where a lightning emission is identifiable at visible wavelengths (D’Aversa et al., this

130 issue). C5 is straddling the terminator and is the first cube containing information on the
 131 dayside ocean and clouds. Some coastlines are identifiable in C4 and C5 at thermal
 132 wavelengths, as it will be discussed in Section 4.4. All the subsequent cubes (C6 to C17) are
 133 acquired in daylight and hence the full spectrum can be investigated, even if they only cover
 134 the ocean surface mostly under cloudy/stormy conditions.

135 Cubes C11, C12 and C13 have been acquired with longer integration times, with the purpose
 136 of testing the instrument response. This leads to signal saturation in many regions
 137 (especially at visual wavelengths over clouds, see Section 2.3.1), that have been removed
 138 from our analysis. The spatial resolution in this dataset is quite stable (about 1.4 km per
 139 pixel, slightly affected by motion smearing) and is suited for the investigation of both
 140 homogeneous and localized cloud structures. On the other hand, the IFOV is affected by
 141 unresolved cloudiness (likely widespread) which dilutes the low reflectivity of deep water
 142 hence preventing the acquisition of clear-sky ocean (Section 2.3.1, Figure 2).

143

144 **Table 1:** MAJIS observing parameters during EGA. Phase angle is always close to 90°.

| | ID | target | incidence angle (°) | emission angle (°) | local time (h) | instantaneous resolution (km/px) |
|-----|----------------|--------------------|---------------------|--------------------|----------------|----------------------------------|
| C1 | 20240820212509 | surface night | 115-130 | 28-42 | 03:00 – 04:18 | 1.80 |
| C2 | 20240820212818 | surface night | 106-116 | 17-27 | 03:54 – 04:48 | 1.55 |
| C3 | 20240820213029 | surface night | 100-106 | 12-19 | 04:30 – 05:12 | 1.50 |
| C4 | 20240820213208 | surface night | 93-100 | 6-13 | 05:00 – 05:36 | 1.45 |
| C5 | 20240820213347 | surface terminator | 87-93 | 0-11 | 05:24 – 06:00 | 1.40 |
| C6 | 20240820213530 | surface day | 82-87 | 6-11 | 05:54 – 06:18 | 1.35 |
| C7 | 20240820213644 | surface day | 79-82 | 11-14 | 06:12 – 06:30 | 1.30 |
| C8 | 20240820213731 | surface day | 72-77 | 17-20 | 06:36 – 07:00 | 1.30 |
| C9 | 20240820213840 | surface day | 71-76 | 14-20 | 06:36 – 07:06 | 1.30 |
| C10 | 20240820214003 | surface day | 64-69 | 24-27 | 07:12 – 07:36 | 1.30 |
| C11 | 20240820214117 | surface day | 56-61 | 32-37 | 07:48 – 08:12 | 1.30 |
| C12 | 20240820214231 | surface day | 55-60 | 29-34 | 07:48 – 08:12 | 1.25 |
| C13 | 20240820214350 | surface day | 46-52 | 39-45 | 08:24 – 08:54 | 1.30 |
| C14 | 20240820214509 | surface day | 34-42 | 50-58 | 09:06 – 09:42 | 1.35 |
| C15 | 20240820214628 | surface day | 36-41 | 49-53 | 09:18 – 09:36 | 1.30 |
| C16 | 20240820214720 | surface day | 26-32 | 60-65 | 10:00 – 10:18 | 1.40 |
| C17 | 20240820214813 | surface day | 23-31 | 60-66 | 10:06 – 10:30 | 1.40 |

145

146

2.2. PRISMA data

147

148 An observing campaign coordinated to the EGA was conducted by the mission PRISMA
 149 (*PR*ecursore *IP*erSpettrale della *M*issione *A*pplicativa), managed by the Italian Space
 150 Agency. The mission hosts a visible and near-infrared imaging spectrometer, covering a
 151 range (400-2500 nm) compatible with the MAJIS-VISNIR channel but having a coarser
 152 spectral resolution (~12 nm) in turn compensated by a higher spatial resolution (~30
 153 m/pixel). Details about the instrument and the mission can be found in Pignatti et al. (2013),
 154 while mission characteristics, access, products, calibration, geometry navigation and data
 155 policy are fully described in Lopinto et al. (2021).

156 PRISMA sequences (13 in total, red rectangles in Figure 1, main parameters summarized in
 157 Table 2) consist of a variable number of 30 x 30 km hyperspectral cubes, each composed of
 158 1000 x 1000 spatial pixels. Due to the PRISMA orbit (Sun-Synchronous-Low-Earth-Orbit),
 159 observations are acquired at a fixed solar local time (~10:30), making it impossible to
 160 achieve spatial/temporal coincidence with MAJIS ones (see next section).

161

162 Table 2: PRISMA observations acquired in coordination with JUICE.

| PRISMA sequence | Num cubes | Start UTC | Solar zenith angle (°) | Emission angle (°) | Cloud coverage (%) | Δt (h) (PRISMA-MAJIS) |
|-----------------|-----------|------------------|------------------------|--------------------|--------------------|-------------------------------|
| 01 | 3 | 2024-08-17 03:34 | 20.3 | 14.6 | 14 | -90.9 |
| 02 | 21 | 2024-08-18 23:13 | 23.4 | 17.1 | 8 | -46.45 |
| 03 | 9 | 2024-08-19 00:50 | 20.6 | 20.7 | 9 | -44.83 |
| 04 | 11 | 2024-08-19 02:22 | 21.4 | 4.2 | 100 | -43.19 |
| 05 | 21 | 2024-08-19 04:08 | 22.7 | 1.2 | 73 | -41.52 |
| 06 | 9 | 2024-08-20 01:07 | 23.6 | 16.6 | 2 | -20.55 |
| 07 | 11 | 2024-08-20 02:46 | 22.5 | 18.4 | 18 | -18.90 |
| 08 | 13 | 2024-08-20 04:25 | 21.0 | 16.0 | 98 | -17.24 |
| 09 | 9 | 2024-08-20 23:46 | 23.2 | 12.3 | 1 | 2.11 |
| 10 | 17 | 2024-08-21 03:03 | 22.0 | 12.0 | 5 | 5.39 |
| 11 | 3 | 2024-08-22 03:19 | 21.7 | 5.6 | 20 | 29.66 |
| 12 | 1 | 2024-08-22 21:07 | 22.2 | 7.6 | 16 | 47.45 |
| 13 | 3 | 2024-08-25 02:32 | 21.6 | 4.3 | 7 | 100.88 |

163

164 2.3. General comparison overview

165

166 Both MAJIS and PRISMA acquired multispectral data covering the same kinds of structures,
 167 offering a useful benchmark for checking MAJIS capabilities in detecting and analyzing
 168 specific features of scientific interest. In the following section we investigate how the spectral
 169 signatures of the main atmospheric gases and of clouds are affected by the different
 170 spatial/spectral resolutions and observing conditions. When reflectances are discussed,
 171 they are obtained for both instruments as I/F , where I is the observed spectral radiance and

172 *F* is Kurucz solar spectral radiance (Kurucz et al., 1984; Kurucz, 1995) available at the
 173 website <https://earth.gsfc.nasa.gov/climate/projects/solar-irradiance/data> (accessed
 174 February, 10, 2026). For readability, in the following we will refer to spectral radiance simply
 175 as *radiance*.

176

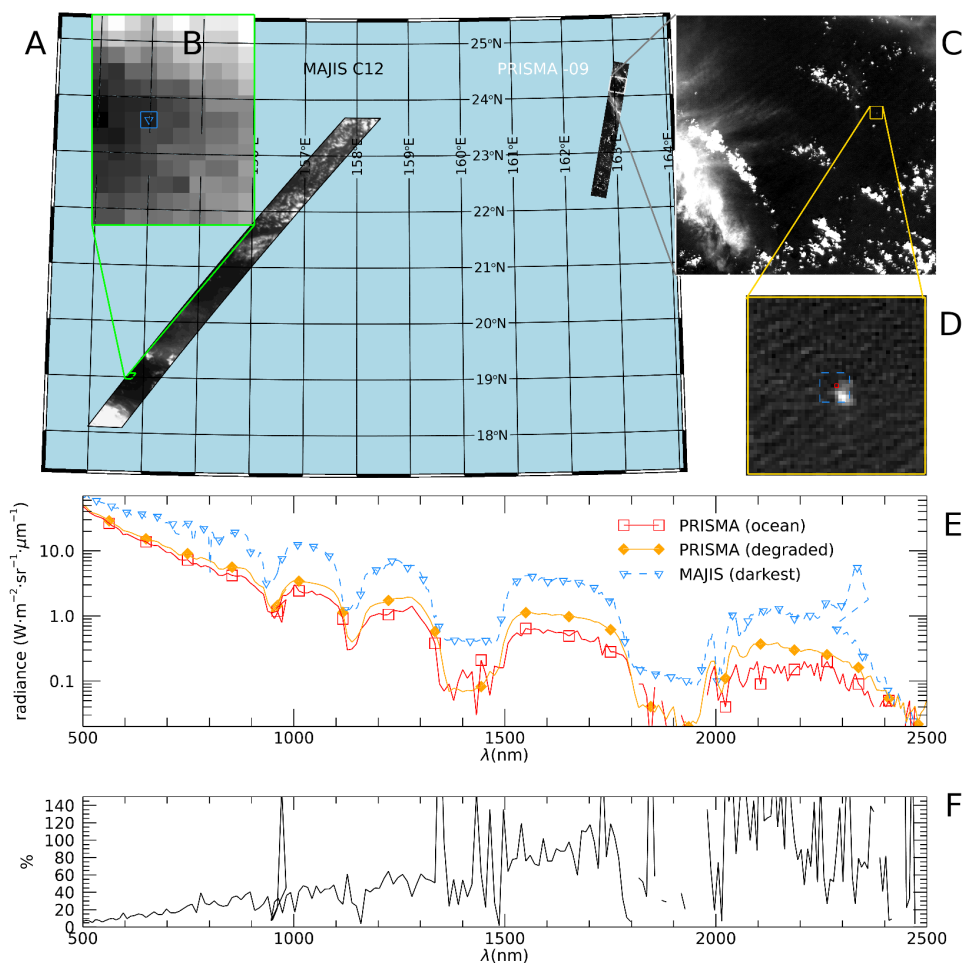
177

2.3.1. Ocean/clouds spectra first comparison

178

179 Figure 2 shows the two PRISMA and MAJIS cubes that are closest from both a spatial and
 180 temporal point of view (~550 km and ~2 h apart), covering open ocean areas overlaid by a
 181 different amount of clouds. In this framework, the most robust radiance comparison should
 182 consider ocean cloud-free spectra, expected to be quite stable in space and time and very
 183 dark at visual wavelengths (given the very low ocean albedo, ~4%). However, the
 184 comparison between the two instruments (Figure 2E) highlights that the darkest MAJIS
 185 signals are still brighter than those from PRISMA, possibly suggesting enhanced
 186 cloud/aerosol content. Indeed, the higher spatial resolution of PRISMA data reveals a
 187 number of small-scale structures, likely unresolved by MAJIS, yet affecting its signal. For
 188 instance, the small bright feature imaged by PRISMA in Figure 2D, covering only a portion of
 189 a MAJIS pixel footprint, may induce spectral variations of the ocean spectrum up to 50%
 190 (Figure 2F) once observed at the MAJIS resolution scale.

191



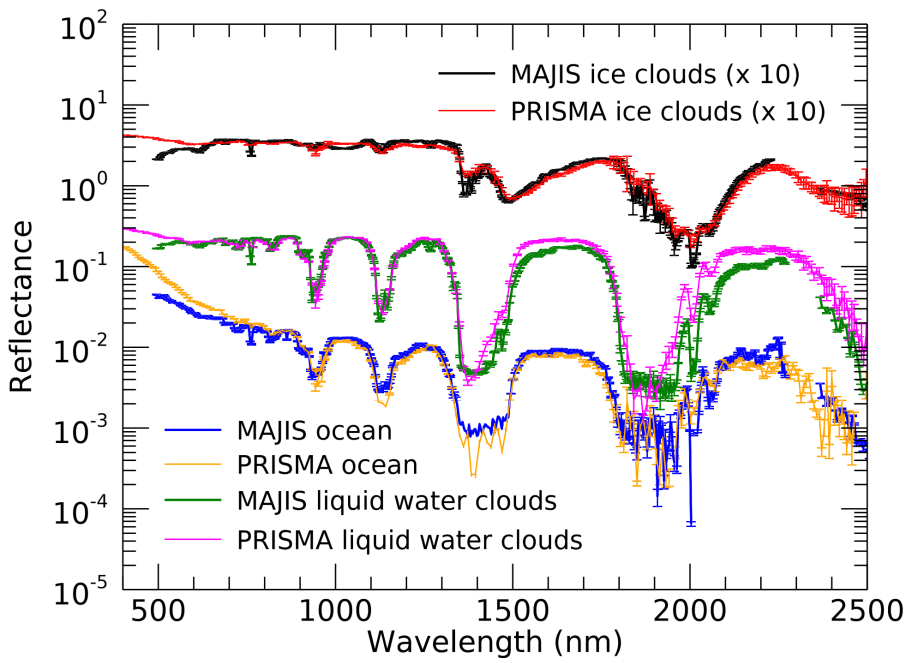
192

193 **Figure 2: A)** MAJIS observation C12 and PRISMA sequence P09 (~2h apart) shown at 875
194 nm in an equal-area projection. **B)** Blow-up of the darkest area in the MAJIS image,
195 highlighting individual pixels' size (the pixel with the lowest signal is highlighted in blue). **C)**
196 The second cube of the PRISMA sequence is shown in its full extension of 1000x1000
197 pixels. **D)** Blow-up of an area of PRISMA data encompassing a small bright cloud. The blue
198 dashed box shows the approximate size of a MAJIS pixel. **E)** Single-pixel spectra from the
199 darkest pixels of MAJIS (blue color, triangle symbol in B) and PRISMA (red curve, red
200 square in D). The orange curve represents a PRISMA spectrum degraded to MAJIS spatial
201 resolution (average inside the blue box of panel D). The MAJIS spectrum is multiplied by the
202 ratio of solar incidence cosines ($=1.82$) to achieve a radiance level comparable with
203 PRISMA. **F)** Spectral effect of the spatial degradation in PRISMA data, shown as the relative
204 difference between the red and orange curves of panel E.

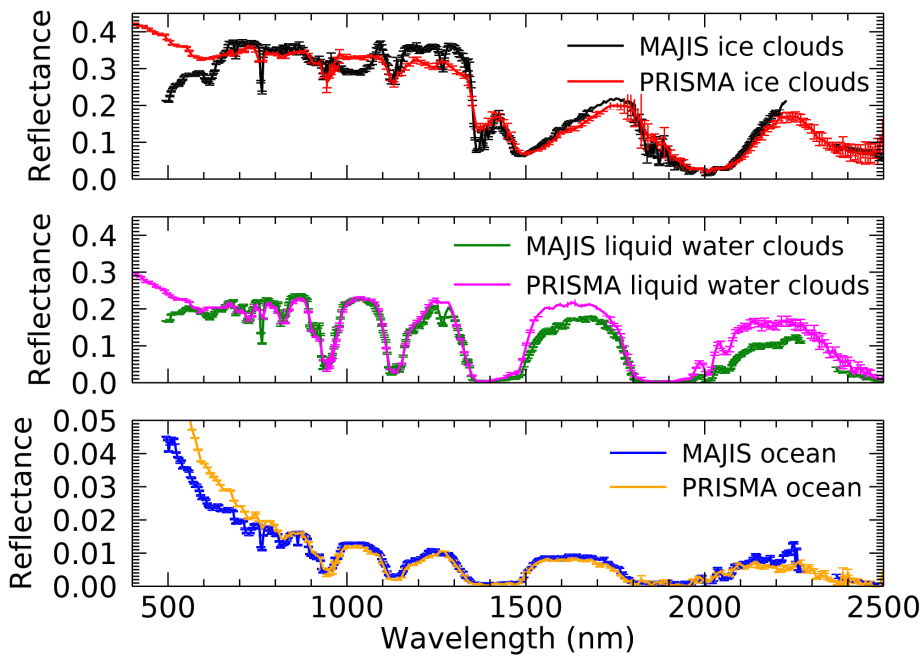
205

206 Most of the spectral variability in both datasets is driven by changes in the H₂O absorption
207 bands. Besides the general low reflectivity, ocean spectra are characterized by the presence
208 of large and often saturated water absorption bands. On the other hand, H₂O clouds (either
209 composed of liquid droplets, ice crystals or a mixture) can easily be identified through RGB
210 imaging from both datasets due to their bright appearance (Section 3.1). H₂O bands are less
211 saturated over clouds, where light scattering prevents photons from reaching the
212 underneath, more absorbing, atmospheric layers. Ice clouds' discrimination is basically
213 driven by the spectral shift of absorption bands between solid and liquid H₂O phase (Section
214 3.1). The comparison of spectral signatures related to the ocean and clouds (main spectral
215 endmembers for both instruments) is shown in Figure 3A-B in log and linear scale
216 respectively (refer to Figures 4 and 5 for the gaseous features identification). This
217 comparison should be considered as qualitative, since spectra acquired at different
218 locations, geometries and local times are being considered (see Tables 1 and 2). Therefore,
219 clouds are likely characterized by different vertical distributions and microphysical properties,
220 driven by a radiative forcing that is changing between early and mid-morning. Also,
221 differential sun-glint effects (dependent on geometry and wind strength) could produce
222 differences in the overall reflectivity of the ocean (Cox and Munk, 1954). All these effects
223 (straylight could also have an impact here, see Langevin et al, this issue) are likely to
224 contribute to non-linear offsets in the continuum below about 700 nm (e.g. Zinner et al.,
225 2016), and slightly different depth and shape of water absorption bands, not ascribable
226 solely to differences in spectral resolution.

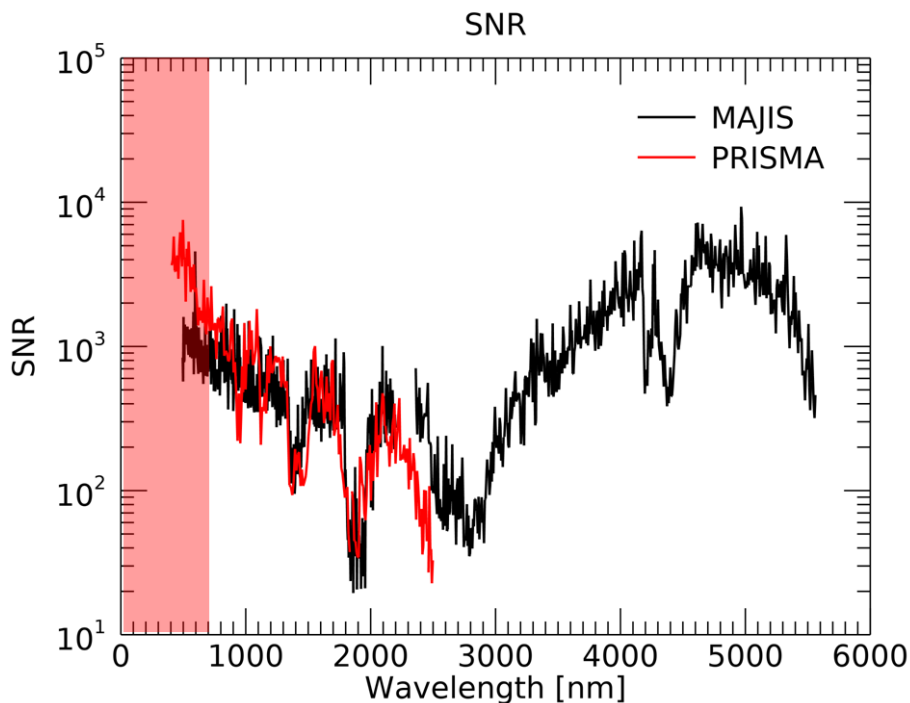
227



228 A



229 B



230 C

231 **Figure 3:** comparison between MAJIS and PRISMA reflectances in log (A) and linear (B)
 232 scales related to ocean, liquid water clouds and ice water clouds (the latter multiplied by 10
 233 for clarity in panel A). PRISMA spectra are selected from two orbits in session 7, MAJIS
 234 ones from orbits C7 (ice clouds) and C10 (ocean and liquid water clouds). Panel C shows
 235 the SNR estimated for the two instruments (cube C15 for MAJIS, one cube of session 07 for
 236 PRISMA) as described in Section 2.3.1. The red shaded area indicates the spectral region
 237 possibly affected by straylight contamination, not yet fully assessed in both datasets.

238

239 The three endmembers in Figure 3 show similar trends in reflectivity, with the main
 240 absorption bands' shape correctly reproduced, even if the probed atmospheric structure is
 241 probably not the same. For example, MAJIS liquid water clouds spectrum shows wider wings
 242 and a flatter bottom for the bands at 1400 and 1900 nm, suggesting different scattering
 243 properties in the atmospheric column for the two cases (see Section 4.2.4). A slightly flatter
 244 bands' bottom is also observed in the ocean spectrum (blue compared to the orange
 245 PRISMA spectrum). On one side, this could indicate that early-morning thin clouds in the
 246 mid-high troposphere are mixed in MAJIS footprint, preventing the formation of the narrower
 247 water lines inside the bands (MAJIS spectrum refers to 7:30 local time, when the presence of
 248 unresolved hazes is likely). On the other hand, such low signals could reach the instrument
 249 noise equivalent spectral radiance (NESR), hence explaining the featureless bands' bottom.
 250 We derived an upper limit for the NESR by investigating the darkest ocean region in the
 251 selected MAJIS cube (C10), resulting in about 10^{-3} W/(m² μm sr) at 1900 nm. This value
 252 corresponds to reflectances of 10^{-4} , about one order of magnitude below the ocean signal at
 253 that wavelength (Figure 3A), hence making the mixed-footprint hypothesis more likely. The
 254 occurrence of saturation in some parts of MAJIS spectrum is highlighted in the ice clouds
 255 comparison, evident as a broad absorption between 900 and 1100 nm in Figure 3B. MAJIS
 256 uncertainties are extensively discussed in the paper by Poulet et al. (this issue), but here we
 257 attempt an *a posteriori* estimation of the spectral signal to noise ratios (SNR) for both

258 instruments by performing a statistical analysis of spatial fluctuations computed in 5x5 pixels
 259 boxes (Figure 3C). For each wavelength (excluding saturated regions) we select those
 260 regions producing the minimum relative error, hence representing both noise statistics and
 261 true variations in the observed scene. As a result, the spectral SNRs in Figure 3C refer to
 262 wavelength-dependent locations in the respective cubes, rather than to a single region. This
 263 means that the high frequency oscillations in the red and black lines are mostly driven by
 264 spatial differences between the selected boxes (at the scale covered by the respective
 265 cubes). Values below ~700 nm (red shaded area in Figure 3C) could be driven by
 266 differences in clouds/aerosols' properties (in turn impacting the intensity of Rayleigh
 267 scattering), and are possibly contaminated by the presence of straylight affecting the actual
 268 trend of the SNR for both instruments.

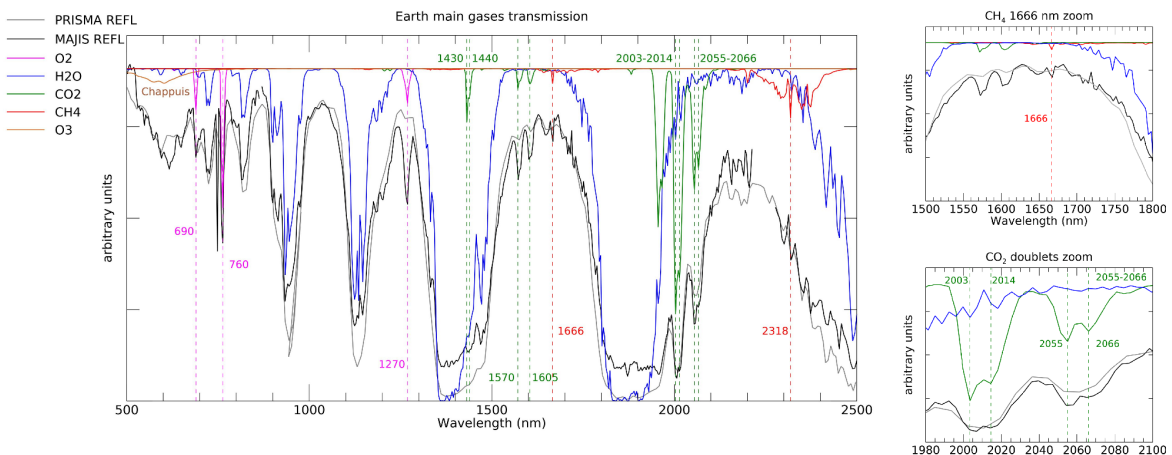
269

270

2.3.2. Gaseous compounds

271

272 Figure 4 compares sample MAJIS/PRISMA liquid water clouds reflectance spectra with
 273 two-way vertical transmission due to O₂, H₂O, CO₂, CH₄, N₂O and O₃, based on an average
 274 vertical structure from Efremenko and Kokahnovsky (2021) and calculated through the
 275 line-by-line method with line parameters from the HITRAN database (Gordon et al., 2022)
 276 and from O₃ cross sections by Gorshchev et al. (2014) and Serdyuchenko et al. (2014).
 277 Finally, transmissions are convolved at the MAJIS spectral resolution.



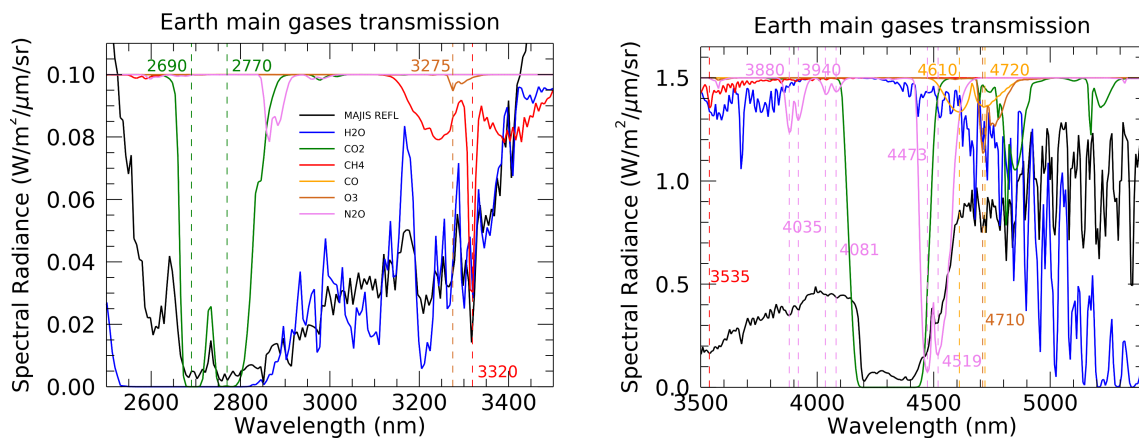
278

279 Figure 4: MAJIS (black, taken from C7) and PRISMA (cyan, taken from session 7)
 280 normalized reflectances (both pertaining to liquid water cloud scenarios) compared to main
 281 Earth's atmospheric gases two-way transmissions convolved on MAJIS spectral grid. Vertical
 282 dashed lines indicate the main non-H₂O molecular lines identifiable in the observations.
 283 Zooms related to the CH₄ 1666 nm absorption line, and the CO₂ doublets at 2003-2014 nm /
 284 2055-2066 nm are shown in the upper and lower right panels respectively.

285

286 In their common spectral range, both instruments allow to identify the main absorption
 287 features of H₂O, O₂ and CO₂ (Figure 4, see also Poulet et al., this issue). The reduced
 288 spectral resolution of PRISMA makes it difficult to resolve narrow features like the methane
 289 absorption at 1666 nm (Figure 4, upper right panel), the close doublets of CO₂ at 2003-2014
 290 nm and 2055-2066 nm (Figure 4, lower right panel), or shallower lines of water. On the other
 291 hand, the PRISMA spatial resolution is expected to reduce the spatial mixing of different
 292 types of surfaces or aerosols, allowing a more robust tracking of localized and transient
 293 phenomena (e.g. smog layers, ice patches, oil spills, CO₂ emissions, etc.). At wavelengths

294 around 600 nm a broad absorption possibly matching the O₃ Chappuis band appears in both
 295 datasets. In MAJIS, this is enhanced over thick clouds and in particular in grazing
 296 illumination conditions (Section 4.4) in which the atmospheric column above ~20 km is
 297 directly illuminated resulting in a very long photon path length that increases the absorption
 298 from O₃ in the scattered light (most of terrestrial ozone resides between altitudes of 20 and
 299 40 km). Nevertheless, a better quantification of this feature requires a more rigorous
 300 assessment of the straylight contamination (Langevin et al., this issue).
 301 Besides the better spectral resolution, MAJIS also has the advantage of an extended
 302 spectral range covering wavelengths from 2500 nm up to 5560 nm. In this range, thermal
 303 emission dominates and provides information on the temperature of the sampled
 304 atmospheric layers, or of the ocean and clouds. This interval is characterized by several H₂O
 305 absorption bands (the stronger one centered at about 2700 nm), strong and saturated CO₂
 306 ones at 2690, 2770 and 4300 nm, and weaker CH₄, O₃, CO and N₂O signatures (Figure 5,
 307 see also Guerlet et al., this issue). In particular, the strong CO₂ absorption (and emission) at
 308 4300 nm, can be used for the estimation of the vertical structure of atmospheric
 309 temperatures (see Poulet et al., this issue).



310
 311 **Figure 5:** MAJIS (black) spectral radiance compared to main Earth's atmospheric gases
 312 two-way spectral transmissions (offset for clarity) in the 2500 - 3500 nm range (left) and
 313 3500-5400 nm range (right). Thermal emission is not considered in the transmission
 314 computation and all spectra are convolved to the MAJIS spectral grid.

315
 316 **3. Methods**

317
 318 In this section we describe different methods for investigating the information content in the
 319 data, including surface/cloud features identification (Section 3.1), ice characterization
 320 (Section 3.2), clouds' altitude estimation (Section 3.3) and high-altitude features investigation
 321 (Section 3.4).

322
 323 **3.1. Surface and clouds identification**

324
 325 In principle, Earth observations can encompass different types of surfaces, commonly
 326 discriminated spectrally through indices expressed in the formalism of *Normalized Difference*
 327 *spectral Indices* (NDIs, see Wolf, 2010 for a general review). Useful examples are given in
 328 Hurley et al., 2014 (dealing with Rosetta/VIRTIS-M data, Coradini et al., 1999) and in Oliva
 329 et al., 2017 (dealing with both Rosetta and Venus Express/VIRTIS-M data, Drossart et al.,

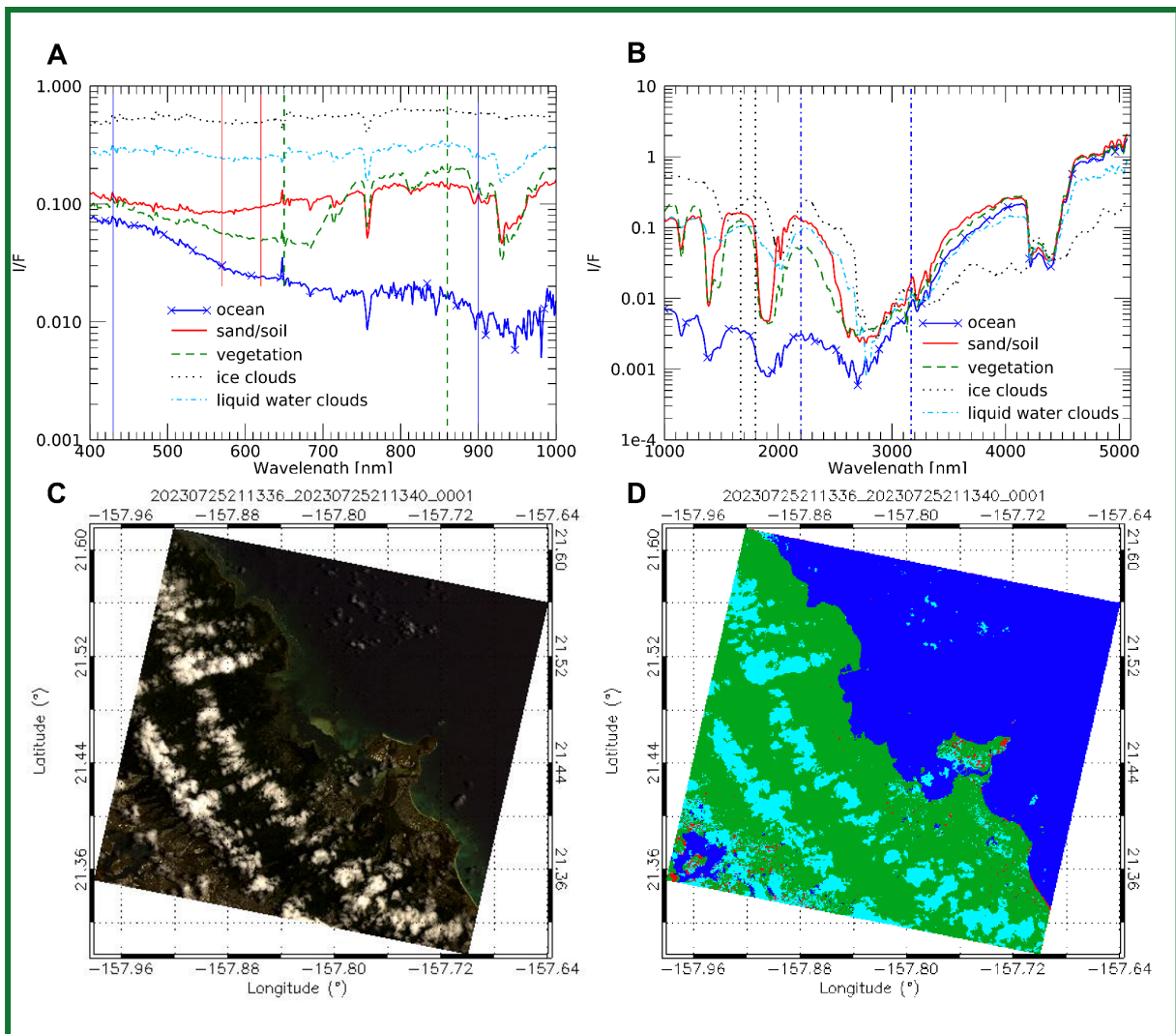
2004). Table 3 summarizes these indices (derived from spectral endmembers from Rosetta/VIRTIS-M acquisitions, Figure 6A-B, since MAJIS observations did not cover surface features in daylight) that we test on PRISMA data (Figure 6C-D) as a benchmark for the future September 2026 EGA, in which Africa observations are planned. A new ocean index is also defined specifically for MAJIS data, which do not cover all wavelengths of the nominal ocean NDI. It is worth stressing that the ocean class should not be considered as representative of clear-sky conditions as it may actually include some amount of aerosol opacity (Section 2.3.1). No specific index has been adopted for generic clouds identification, but we rather assign to this class all pixels that do not meet any of the surface classes' conditions. Indices thresholds can be studied taking advantage of proxy images (e.g. the PRISMA one shown in Figure 6C, not pertaining to EGA sequence) in which the changing reflecting structures can be clearly identified. The derived values depend on instrument features and require specific tuning when switching between different datasets. Figure 6C-D shows how the different types of spectral classes can be reliably identified, even if, in this case, no ice clouds are present. Other examples of application of the ocean, clouds and ice indices from Table 3 to MAJIS and PRISMA data are discussed in Section 4.1. Instead, the application of surface-related indices to MAJIS data did not result in positive identification, since land features in MAJIS data are not seen in daylight illumination, making NDIs not applicable.

349

| SPECTRAL CLASS | SPECTRAL INDEX | SPECTRAL SIGNATURE | FIGURE |
|--------------------|---|--|----------------|
| Vegetation | $NDVI: \frac{R_{860} - R_{650}}{R_{860} + R_{650}}$ | Chlorophyll absorption in the red band | 6D |
| Sand/Soil | $NDSI: \frac{R_{570} - R_{620}}{R_{570} + R_{620}}$ | Enhanced contrast between the red and green bands | 6D |
| Ocean | $NDWI: \frac{R_{430} - R_{900}}{R_{430} + R_{900}}$ | Enhanced reflectivity in the blue with respect to NIR wavelengths | 6D - 12D |
| <i>MAJIS Ocean</i> | $\frac{R_{2200}}{R_{3170}}$ | Low solar I/F, large thermal emission | 12C |
| Ice Clouds | $\frac{R_{1670}}{R_{1800}}$ | Shift of the 1500 nm H ₂ O ice absorption band to longer wavelengths with respect to the liquid phase (different arrangement of hydrogen bonds) | 12C - 12D |
| Cloudy | pixels not assigned to surface types | / | 6D - 12C - 12D |

350

351 **Table 3.** Spectral indices for the identification of different spectral classes related to surfaces
352 and clouds. *R* indicates I/F and the subscript is the wavelength in nanometers.



353

354

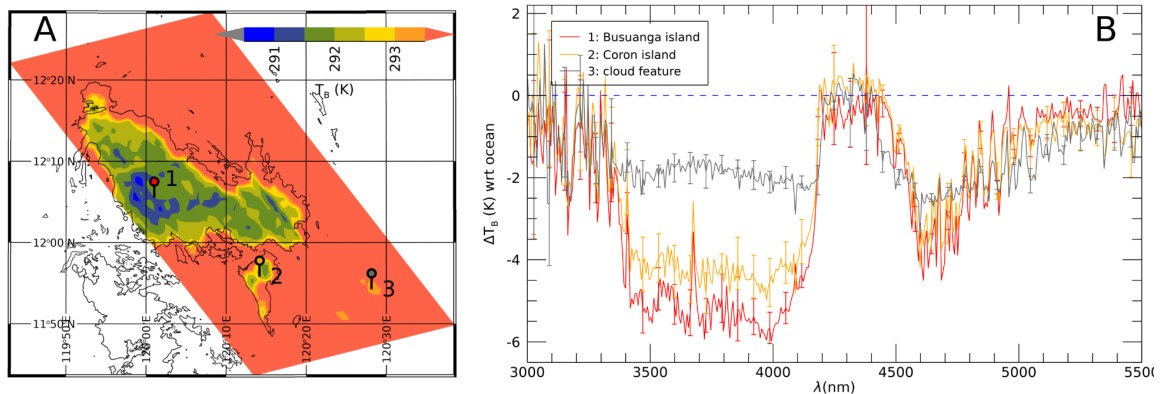
355 **Figure 6:** **A:** Reflectance endmembers of different classes of surface and clouds, derived
 356 from Rosetta/VIRTIS-M VIS channel Earth observations (Oliva et al., 2017). Vertical dashed
 357 lines share the style and color of the corresponding spectral endmember and identify the
 358 wavelengths adopted in the index definition (blue ones refer to the NDWI). **B:** same as in A
 359 but I/F spectra from the NIR channel of VIRTIS-M are shown (vertical blue dashed-dotted
 360 lines refer to the MAJIS ocean index). **C:** Example of a PRISMA RGB image covering
 361 different surface types (data cube 2023072521336_20230725213340) targeting the eastern
 362 coastal line of Honolulu island ($R=680$ nm; $G=570$ nm, $B=440$ nm). **D:** distribution of spectral
 363 classes obtained from the spectral indices in Table 3. Green pixels indicate vegetation, red
 364 ones are sand, cyan ones are clouds, blue ones indicate ocean/water (no ice clouds
 365 present).

366

367 In the specific conditions of MAJIS EGA sequence, the most robust land identification must
 368 rely on soil/ocean contrast in thermal emission (Section 4.4), triggered by the different
 369 thermal inertia of the two classes. However, also the presence of clouds in the line of sight
 370 induces a decrease of the observed brightness temperature (T_B), hence land identification
 371 requires matching the shapes of low T_B regions within known coastlines. The largest land
 372 region emerging in this way is shown in Figure 7 (cube C4), (Philippines's Busuanga and
 373 Coron islands in cube C4), whose identification also allows a refinement of MAJIS pointing

374 reconstruction (Seignovert et al., this issue). The largest brightness temperature contrast for
 375 both land/ocean and cloud/ocean cases occurs in the 3500-4000 nm and 4600-4800 nm
 376 spectral ranges, which are less absorbed by atmospheric H₂O and CO₂. The application of
 377 this method to other MAJIS data is illustrated in more detail in Section 4.4.

378



379

380 *Figure 7: Land detection obtained by comparing the shapes of low brightness temperature*
 381 *(T_B) regions in MAJIS cube C4 with known coastlines. **A)** Identification of Busuanga and*
 382 *Coron islands (markers 1 and 2 respectively), colder than the surrounding ocean, as well as*
 383 *clouds (marker 3). **B)** Spectral contrast in brightness temperature (T_B) with respect to the*
 384 *ocean spectrum, measured over the islands (Busuanga in red, Coron in orange) and over a*
 385 *thin cloud (grey curve). Coastlines data from OpenStreetMap, available under the Open*
 386 *Database License.*

387

388 3.2. Ice characterization

389

390 MAJIS and PRISMA data allow investigating the distribution of physical properties of ice and
 391 how they relate, for example, to the altitude of the clouds where it is identified (see Sections
 392 4.1 and 4.2). The temperature, crystallinity, grain size, purity, and density affect the shape of
 393 ice absorption bands (in particular the main ones at 1500 nm and 1900 nm) and of the
 394 continuum. Since the long wavelength shoulder of the 1900 nm band encompasses the
 395 noisy junction between the VISNIR and IR channels of MAJIS, we focus on the 1500 nm
 396 band, spectrally well resolved in both MAJIS and PRISMA datasets. This band has a
 397 characteristic asymmetry (due to its differential intensity with respect to the 1900 nm one,
 398 e.g. Stephan et al., 2021) affecting the position and shape of the in-between transmission
 399 window peak (~1700 nm) and has been used for the definition of the ice index in Table 3.
 400 Within the 1500 nm band, the weaker 1650 nm absorption is present. Its strength is a proxy
 401 for the degree of the ice crystallinity and temperature (Fink and Larson, 1975; Filacchione et
 402 al., 2016). It is also observable in PRISMA, even if shallower and noisier due to the lower
 403 spectral resolution (see zooms in Figure 8A and B).

404 The 3000 - 4000 nm wavelength range, not accessible to PRISMA, hosts two ice reflection
 405 peaks at around 3100 nm (the Fresnel peak) and 3700 nm (Figure 8C). The former varies in
 406 shape and intensity as a function of the ice crystallinity (Cartwright et al., 2025) while the
 407 latter shifts to longer wavelengths as temperature increases (e.g. Filacchione et al., 2016,
 408 see Section 3.3.3). Fresnel peak position variations are estimated in the data through
 409 cross-correlating each ice spectrum with a constant shape (average peak shape in each
 410 cube) which is rigidly shifted with a 0.1 nm sampling (hence allowing the estimation of the
 411 peak with a sampling better than the nominal MAJIS one). On the other hand, the 3700 nm

412 peak position is obtained through fitting with a Gaussian function, reliably reproducing its
413 shape.

414 Another proxy of the ice temperature is the intensity of its thermal emission, becoming
415 significant at wavelengths larger than 4500 nm (Figure 8D). However, in this range the
416 emitted radiance is absorbed by a plethora of narrow bands of gaseous water, and therefore
417 only a narrow transmission window around 4600 nm is suitable for this purpose. Table 4
418 summarizes these ice spectral features, identifiable in MAJIS and PRISMA data. The
419 average uncertainties Δ are propagated taking into account the SNR estimates described in
420 Section 2.3.1.

421

422

| ICE PARAMETER | Δ MAJIS | Δ PRISMA | ICE PROPERTIES |
|---|----------------------------------|-----------------|------------------------------------|
| 1500 nm band depth | < 1 % | < 1 % | number density / grain size |
| 1500 nm band asymmetry | < 2 % | < 3 % | grain size / crystallinity |
| 1650 nm band depth | 10 % | 20 % | crystallinity |
| <i>Fresnel peak position</i> <i>Fresnel peak intensity</i> | <i>2 nm</i> <i>< 1 %</i> | <i>/</i> | <i>temperature / crystallinity</i> |
| <i>3700 nm peak position</i> <i>3700 nm peak intensity</i> | <i>0.2 nm</i> <i>< 1 %</i> | <i>/</i> | <i>temperature / crystallinity</i> |
| <i>4600 nm thermal intensity</i> | <i>< 1 %</i> | <i>/</i> | <i>temperature</i> |

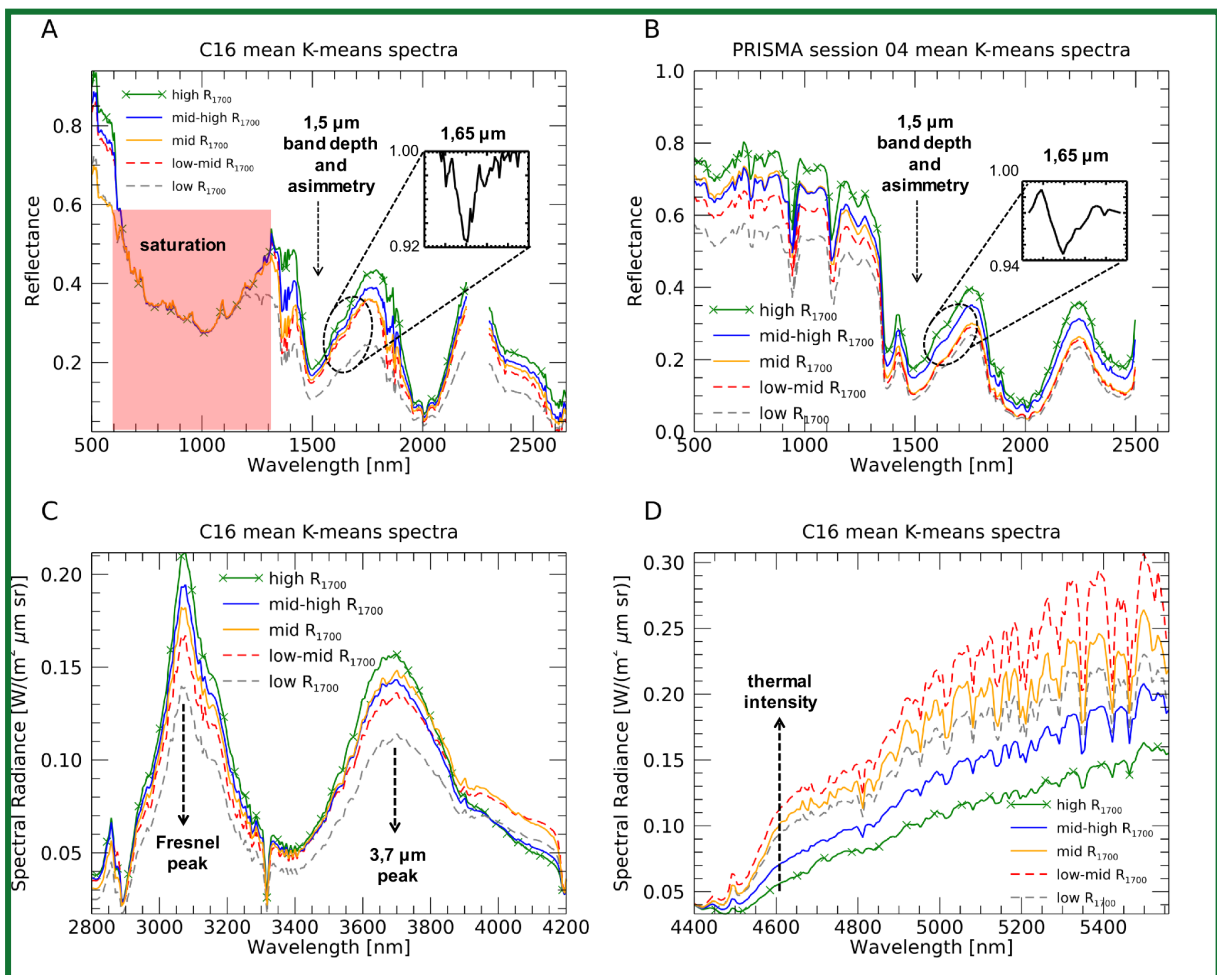
423 Table 4: investigated ice spectral parameters and related average uncertainties (Δ) and ice
424 properties. Cells in light blue indicate parameters that only refer to MAJIS dataset.

425

426 As a first investigation of the ice spectral variability in MAJIS and PRISMA observations we
427 take advantage of the unsupervised K-means classification algorithm included in the ENVI
428 software package, version 6.0 (Exelis Visual Information Solutions, Boulder, CO, USA,
429 <https://www.nv5geospatialsoftware.com/Products/ENVI>, accessed December, 15, 2025).
430 This algorithm is capable of grouping the observations into an ensemble of “K”
431 non-overlapping clusters, driven by spectral similarity, whose average spectra are
432 representative of the main signatures in the dataset. This is done through an iterative
433 minimum distance technique whose details are described in Tou and Gonzalez (1974). In
434 this preliminary analysis, we arbitrarily set the algorithm to produce K=5 output average
435 spectra, enough for visualizing the variability of the main ice diagnostic spectral features. It
436 must be noted that, since we are also interested in features pertaining to infrared
437 wavelengths, in MAJIS case the full VISNIR+IR spectral range is considered, and
438 wavelengths longward of 2500 nm contribute to the clustering as well. As we will see in
439 Section 4.1, this also has an impact on the spatial distribution of the clusters. The resulting
440 average spectra in the solar range are shown in Figure 8A and Figure 8B for MAJIS cube
441 C16 and for one of PRISMA session 04 cubes respectively. These spectra result to be
442 mainly driven by the changing intensity of the continuum, in turn providing information about
443 the opacity of the ice clouds. The color scale is associated with increasing reflectance of the
444 transmission window at 1700 nm (dashed grey, dashed red, orange, blue and green with
445 crosses from low to high, indicating increasing opacity and variable crystal sizes). The same

446 color scheme is retained for the intensity of Fresnel peak at 3100 nm in MAJIS data (Figure
 447 8C), diagnostic of the ice crystallinity. Instead, spectra with intermediate reflectances at 1700
 448 nm switch order within the 3700 nm ice reflectivity peak (dashed red to blue to orange from
 449 low to high, Figure 8C) indicating the increased weight of thermal emission on the overall
 450 signal in this range. At MAJIS wavelengths larger than 4500 nm (Figure 8D) the initial color
 451 scheme is totally disrupted, due to the mixing of information about cloud emissivity, cloud
 452 temperature (i.e. the altitude) and gaseous opacity. The combination of high NIR
 453 reflectances and low thermal emission (green spectrum with crosses) suggests the presence
 454 of optically thick high-altitude clouds, as confirmed by the shallower water absorption bands
 455 longward of 4900 nm. On the other hand, large thermal radiance and deep water bands
 456 associated with intermediate NIR reflectance (dashed red spectrum) indicate a population of
 457 moderate opacity clouds at quite low altitudes. The other spectra present intermediate
 458 properties in the thermal range, not strongly correlated with the NIR reflectance, calling for
 459 mixed-phase clouds of variable microphysical properties and vertical structure.

460
 461



462
 463 **Figure 8:** **A:** mean reflectance spectra from the K-means clustering algorithm for MAJIS
 464 cube C16 ($\lambda < 2500$ nm). The red shaded area indicates wavelengths that are saturated due
 465 to the high reflectivity of clouds. Colors indicate different regimes of the continuum
 466 reflectance, taken as reference at the 1700 nm transmission window (R_{1700}). **B:** same as in
 467 A but for PRISMA session 04 (full spectral range). The insets in **A** and **B** zoom between
 468 1570 and 1780 nm to show the average 1650 nm band normalized to the continuum. **C:**

469 MAJIS radiances in the $2800 < \lambda < 4200$ nm range, zooming on the Fresnel and 3700 nm ice
470 reflectivity peaks. **D**: thermal part of the spectrum longward of 4400 nm. In all panels,
471 dashed arrows highlight diagnostic spectral features of the ice.

472

473 **3.3. Estimation of clouds' altitude**

474

475 The most straightforward method for evaluating cloud altitudes involves the correlation of the
476 brightness temperature at a given wavelength (e.g. 4610 nm, less affected by gaseous
477 absorption in the MAJIS range) with a known vertical temperature profile. For ice clouds,
478 temperatures can be derived from the 3700 nm peak position (Section 3.3.3). Other methods
479 that we consider here are based on O₂ absorption bands' variability and on the analysis of
480 clouds' shadows (Sections 3.3.1 and 3.3.2). In this study, we rely on a fixed average
481 temperature profile (Efremenko and Kokhanovsky, 2021), which may be not representative
482 of the actual thermodynamic conditions of the atmosphere during the observations. As a
483 consequence, all the methods that we adopt yield a range of results, each affected by their
484 own intrinsic limitations. Although they appear quite consistent with each other, more
485 quantitative investigations are postponed to future analyses.

486

487 **3.3.1. O₂ band depth variability**

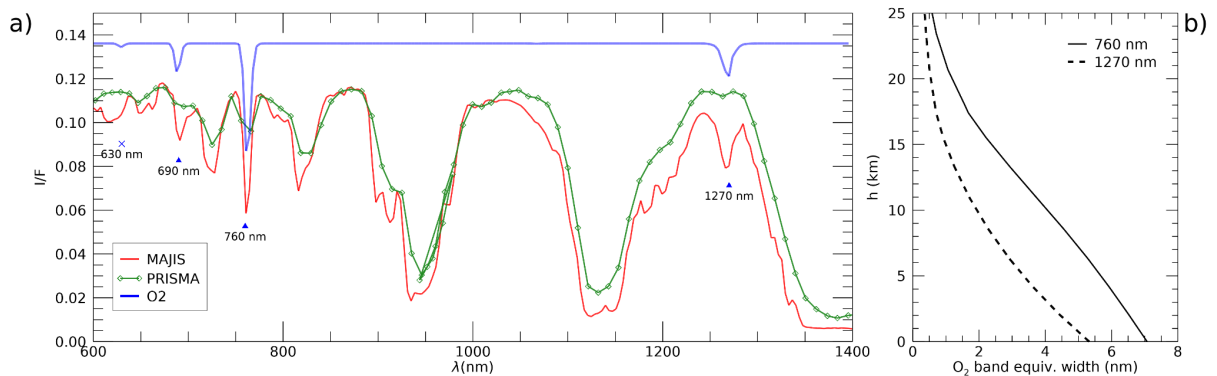
488

489 The O₂ spectral features covered by both MAJIS and PRISMA observations consist of the
490 absorption bands at 630 nm, 690 nm, 760 nm and 1270 nm (Newnham & Ballard, 1998;
491 Smith & Newnham, 1999). As we can see in Figure 9A, MAJIS can resolve all bands except
492 the 630 nm one, while PRISMA data can only partially resolve the 760 nm one. The
493 strongest 760 nm band is the most used from satellite measurements in the near-infrared
494 (e.g. GOSAT, Butz et al., 2011; SCIAMACHY, Bovensmann et al., 1999; TROPOMI, Veeffkind
495 et al., 2012; OCO-2/3, Eldering et al., 2019) for inferring bulk atmospheric quantities like
496 temperature profile, airmass (Stevens et al., 2017), aerosol and clouds properties (Geddes &
497 Bösch, 2015). O₂ is a well-mixed component of the atmosphere, hence the curves of growth
498 of its absorption bands with altitude in the presence of optically thick clouds can be
499 translated into the altitude of the cloud top (e.g. Wei et al., 2024).

500 In our analysis we applied a simplified scheme for retrieving cloud top altitudes from the 760
501 nm band in the PRISMA case and from both 760 and 1270 nm O₂ bands for MAJIS data.
502 The different strength of the two bands implies a different curve of growth with altitude
503 (Figure 9B), with the 1270 nm one less sensitive to higher clouds but more suitable for
504 characterizing lower structures. The 630 and 690 nm bands, intrinsically weaker and more
505 sensitive toward the surface, are not used in this analysis.

506 The comparison of a measured O₂ band depth with its theoretical curve of growth, evaluated
507 for the actual airmass, allows us to directly retrieve the cloud top altitude (Section 4.2.1). It is
508 worth stressing that although altitude, pressure and temperature of the cloud top are
509 important atmospheric parameters (Nakajima et al., 2019), our simplified scheme neglects
510 details of vertical distributions and scattering properties, introducing possible biases in the
511 retrieved absolute values. Propagating the MAJIS uncertainties previously discussed
512 (Section 2.3.1) and assuming suitable model ones (~10% on the oxygen vertical profile
513 induced by local changes in gaseous temperature, density, humidity), errors on cloud top
514 altitude average to values of ~1 km, for both the 760 and 1270 nm bands. In addition, the
515 1270 nm band is known to contain a significant airglow emission feature that can alter the

516 band depth and introduce further biases in the oxygen absorption evaluation (Kuang et al.,
 517 2002).
 518



519
 520 Figure 9: **A)** Typical appearance of O₂ features in the spectra of MAJIS (red) and PRISMA
 521 (green). Modeled spectral transmittance (in blue) highlights location and shape of the O₂
 522 bands at 630, 690, 760, and 1270 nm. Only the last three can be detected in MAJIS spectra
 523 (red curve), while only the strongest 760 nm band is identifiable in PRISMA spectra (red
 524 curve). **B)** Examples of curves of growth of the O₂ absorption at 760 (solid curve) and 1270
 525 nm (dashed curve) in the standard clear-sky atmospheric column adopted in this work. The
 526 absorption is shown as band equivalent width for a 2-ways path with generic incidence and
 527 emission angles of 30°.

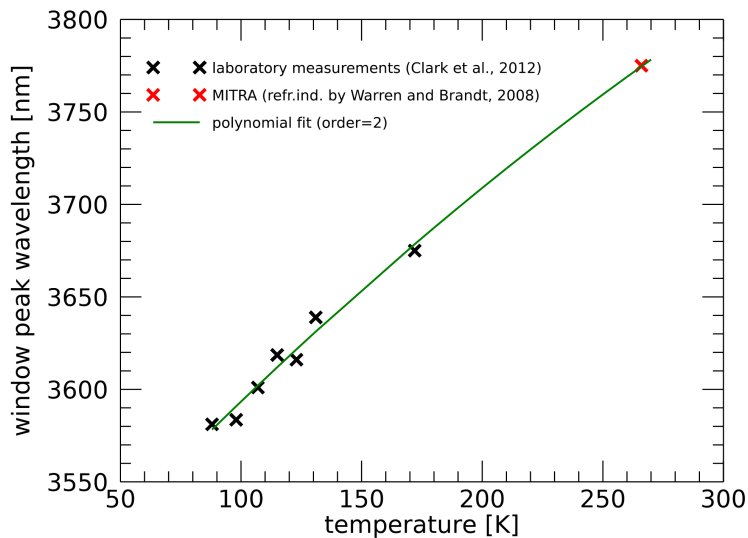
528
 529 **3.3.2. Cloud shadows analysis**

530
 531 The length of projected clouds shadows gives an estimate of their altitude, provided that the
 532 illumination geometry is well known. Significant lengths of projected shadows are more
 533 easily seen in the case of tall convective clouds in slant solar illumination. In the MAJIS case,
 534 clear shadows have been identified for strong convective events surrounded by widespread
 535 background clouds, hence their length can only give hints on relative altitudes (see Section
 536 4.2.2). Here we adopted the simplest assumption of homogeneous cylindrical shapes
 537 (without accounting for the actual three-dimensional density distribution) to estimate the
 538 height of clouds' top with purely geometrical considerations. Under these hypotheses the
 539 associated uncertainties are mainly driven by errors in edge detection (for both cloud and
 540 shadow edges) and, as a consequence, are limited by the spatial resolution. Errors on solar
 541 incidence angle may also play a role in very slant illumination, and the total relative
 542 uncertainties estimated in the conditions of MAJIS observations range between 6 and 10%.
 543 The application of the method is shown in Section 4.2.2.

544
 545 **3.3.3. Derivation of clouds' altitude with the ice temperature**

546
 547 We apply to Earth's icy clouds the same method by Filacchione et al. (2016), who estimated
 548 the temperatures of Saturn's icy satellites surfaces from the displacement of the 3700 nm ice
 549 peak, deriving from a shift of the imaginary part of the ice refractive (Mastrapa et al., 2009).
 550 In that method, temperature-dependent peak reflectivities were derived from laboratory
 551 measurements by Clark et al. (2012), spanning between 88 and 172 K, a range too low to
 552 describe Earth troposphere where clouds are commonly observed. We extrapolate the
 553 peak-temperature dependence by also simulating the ice reflectivity at 266 K, i.e. the
 554 temperature of the optical constants by Warren and Brandt (2008). Since the ice grain size

555 has little effect on the peak position (Filacchione et al., 2012) we assume an effective radius
556 of 20 μm , representative of cirrus clouds (LeMone, 1988). The resulting trend covering from
557 88 to 266 K is shown in Figure 10 (black and red crosses). It is reliably fit with a
558 second-degree polynomial (green line) and can be used for a qualitative estimation of the ice
559 temperature in MAJIS observations (Section 4.2.3).
560



561

562 **Figure 10:** correlation between ice temperature and 3700 nm reflectivity peak position. Black
563 crosses represent laboratory measurements by Clark et al. (2012), the red cross indicates an
564 RT simulation performed with ice grain size of 20 μm and optical constants by Warren and
565 Brandt (2008), and the green line represents a second degree polynomial fit of all data (see
566 Section 3.3.3).

567

568 3.3.4. Forward RT modeling on liquid and ice H₂O clouds;

569

570 The most accurate method for determining clouds' vertical distribution is through full RT
571 modeling. However, this would require a time-consuming retrieval of physical quantities that
572 is beyond the scope of this paper. Instead of spectral inversion, we here perform a
573 comparison of selected observations (i.e., those in Figure 3) with forward RT models
574 obtained by manually tuning aerosols' physical parameters. The derived quantities are to be
575 considered as orders of magnitude of the altitude and microphysical properties of Earth's
576 clouds and aerosols. Forward models are produced with the MITRA RT tool (Oliva et al.,
577 2016; 2018; Sindoni et al., 2017; D'Aversa et al., 2022), adopting the optical constants from
578 Hale and Query (1973), Warren and Brandt (2008) and Kitamura et al. (2007) for computing
579 the scattering properties of liquid water, water ice and silicate minerals (assumed as
580 background aerosol), respectively. The spectral albedo of the ocean is taken from the
581 ASTER spectral library (Baldrige et al., 2009). In this simplified scheme, we neglect thermal
582 emission, discarding measurements longwards 3000 nm.

583 It is interesting to note that, even if beyond the scope of this paper, more accurate RT
584 modeling could also be considered for the evaluation of straylight contamination (studied for
585 MAJIS in Langevin et al., this issue), as it offers the possibility to extrapolate information
586 from the NIR part of the spectrum to visible wavelengths.

587

588 **3.4. High altitude emissions and atmospheric waves identification**

589

590 Among the many gaseous features observable in the 4000-5500 nm MAJIS range, two are
591 particularly interesting, being observed as emission bands. These are the CO₂ double-peak
592 at the bottom of the main 4300 nm band and an O₃ signature around 4700 nm. Both are
593 evident above optically thick clouds at high altitudes, blocking the thermal contribution from
594 the surface and lower (hotter) atmospheric layers. The CO₂ peak is radiometrically much
595 more stable than other spectral features against variation of atmospheric structures (see
596 Poulet et al., this issue). It is known to result from the combination of a LTE component
597 induced by temperature increase in the stratosphere, and a non-LTE one due to the CO₂
598 excitation primarily induced by direct solar pumping occurring at even higher altitudes (where
599 collisional quenching is no longer efficient, e.g. Cassini et al., 2025). The detailed analysis of
600 this emission feature in MAJIS data, implying the evaluation of CO₂ vibrational temperature
601 vertical profiles, is far beyond the purpose of this work. In any case, the spatial distribution of
602 the CO₂ emission intensity can provide interesting insights about the probed layers, and we
603 can indeed use it for detecting atmospheric waves and provide hints about their altitude and
604 propagation (see Section 4.3.1). CO₂ emission can be identified already in MAJIS
605 monochromatic frames at 4270 nm (i.e. the position of the main peak of the emission) but
606 the integration of the band in a narrow spectral range is useful for reducing noise and
607 enhancing the contrast in waves' investigation (Section 4.3). For the integration we consider
608 wavelengths between 4254 and 4333 nm, which probe high altitudes in the atmosphere and
609 are not affected by the thermal contribution from lower ones. Considering the SNR estimated
610 at these wavelengths (Figure 3C), we are able to detect waves whose relative intensity
611 between crests and troughs is about 1%, assuming a 3-sigma uncertainty for the radiance at
612 4270 nm.

613 On Earth, ozone has a maximum density in the lower stratosphere but its vertical distribution
614 strongly depends on latitude (see for example Bekki and Lefevre, 2009). It is produced
615 through a very fast and exothermic 3-body recombination reaction that includes O and O₂ in
616 the presence of a catalytic species (either N₂ or O₂). Aside from diagnostic bands at UV
617 (outside MAJIS domain) and VIS wavelengths (the Chappuis band discussed in Section
618 2.3.2), the 4700 nm one is the strongest feature clearly detectable within the MAJIS range.
619 This O₃ band is seen as either an absorption or emission feature in MAJIS nadir-looking
620 observations, depending on the overall thermal emission of the atmospheric column. In clear
621 sky conditions, when the emission from lower warmer layers is dominant, the O₃ 4700 nm
622 band is hardly detectable being overcome by water absorption (as shown in Poulet et al., this
623 issue), unless radiative transfer modeling is performed on the data (e.g. Guerlet et al., this
624 issue). In the presence of mid-altitude clouds, a shallow O₃ band appears in absorption,
625 while the obstruction of the densest part of the atmospheric column due to high-altitude
626 clouds makes the O₃ band appear in emission. Given this phenomenology, in this preliminary
627 study we investigate the O₃ emission amplitude through the difference between brightness
628 temperatures estimated at 4717 nm (strongest O₃ line) and 4660 nm (outside O₃ band). Such
629 a difference is positive when the O₃ is spectrally observed in emission, negative otherwise.

630

631

632 **3.4.1. Atmospheric waves characterization**

633

634 Atmospheric gravity waves are observed in almost all the MAJIS acquisitions (see examples
635 in Section 4.3.1) at the wavelengths of the central peak of the 4300 nm CO₂ band. Due to the
636 limited field of view, wave packets are usually not visible in their entirety and it is not possible
637 to identify the same wavy structures from one image to the other due to the large coverage
638 gaps, preventing the study of the wave speed propagation. Nevertheless, we attempt to
639 quantify wave properties and provide some hints on their altitude. The wave parameters -
640 horizontal wavelength, total packet length, azimuthal extent, and packet width - are
641 determined through visually processing each image. Automated methods were not possible
642 because of the variability in images' contrast. After appropriate image stretching, the
643 wavefronts are identified by tracing the crest lines. The horizontal wavelength is defined as
644 the average distance between consecutive crests within each wave packet. The total packet
645 length is measured as the distance between the first and last identified crests. The azimuthal
646 extent is derived from the common orientation of the crests counted counterclockwise, while
647 the packet width is defined as the maximum crest length among those identified. Taking into
648 account spatial resolution and signal contrast, uncertainties in size estimation are of about 7
649 km, while those on wavelengths are less than about 11 km.

650 Circular-wave patterns have been observed in some MAJIS images, likely resulting from the
651 breaking of upward-propagating waves originating in sufficiently strong convective
652 thunderstorms. Under this assumption, we attempt to infer the time delay between the
653 wave-triggering event and its observation (Taylor and Hapgood, 1988; Dewan et al., 1998;
654 see Section 4.3.1). This is done by neglecting wind transport and assuming a simplified
655 isothermal dispersion relation (Hines, 1960) in which the wave speed is negligible with
656 respect to the speed of sound. For circular waves we also measured maximum radius and
657 expansion speed. Because only a portion of the circle is visible in the images, the wave
658 radius is inferred from the following formula:

$$659 \quad r = f/2 + c^2/8f \quad (1)$$

660 where f is the sagitta and c is the chord, observed in the images in pixels and converted to
661 km using the instantaneous resolution in km/px reported in Table 1. The waves are assumed
662 to occur at 15 km height, based on estimations of the brightness temperature of CO₂
663 emission at 4300 nm, used as a proxy for these features. Following the formulation in Taylor
664 and Hapgood (1988) and Dewan et al. (1998), the wave period τ and expansion speed v_{gx}
665 can be obtained using the following formulas:

$$666 \quad \tau^2 = \tau_B^2 [(1 + 1/(\tan\phi)^2)] \quad (2)$$

$$667 \quad v_{gx} = (\lambda_x/\tau) [1 - (\tau_B/\tau)^2] \quad (3)$$

668 with ϕ being the elevation angle identified by the wave propagation direction, $\lambda_x =$
669 wavelength of the propagating wave, and $\tau_B =$ buoyancy period, the latter assumed to be
670 equal to 5 min, which is a good approximation at stratospheric altitude (Dewan and Good,
671 1986).

672

673 4. Results and discussion

674

675 We now present the results we obtain through the application of the methods discussed in
676 Section 3. Section 4.1 provides a discussion on ice properties, Section 4.2 focuses on the

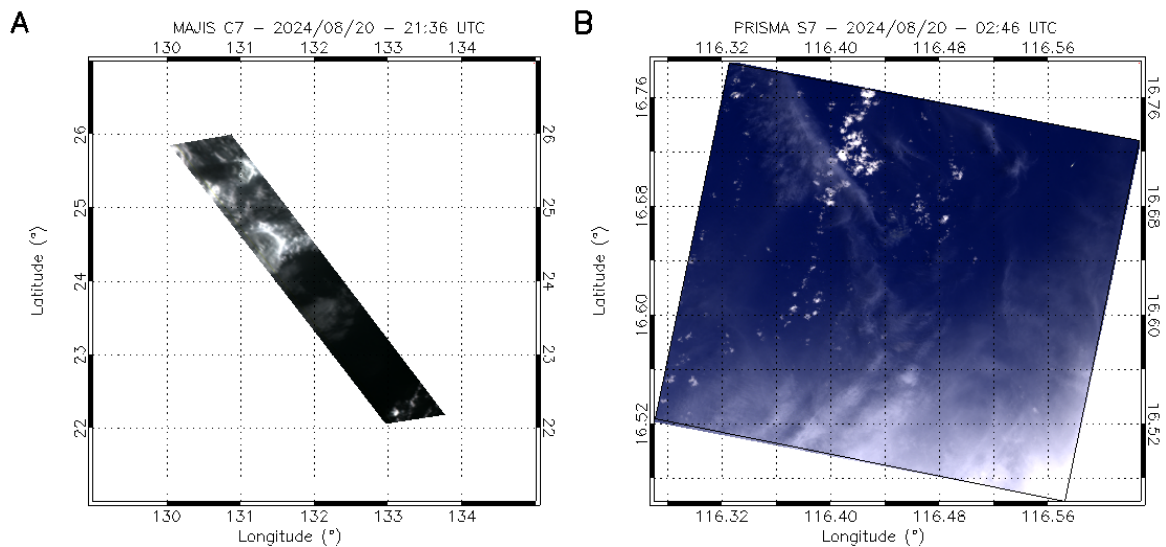
677 clouds' altitudes, Section 4.3 is devoted to high altitude features and Section 4.4 presents
678 results on land features identification.

679

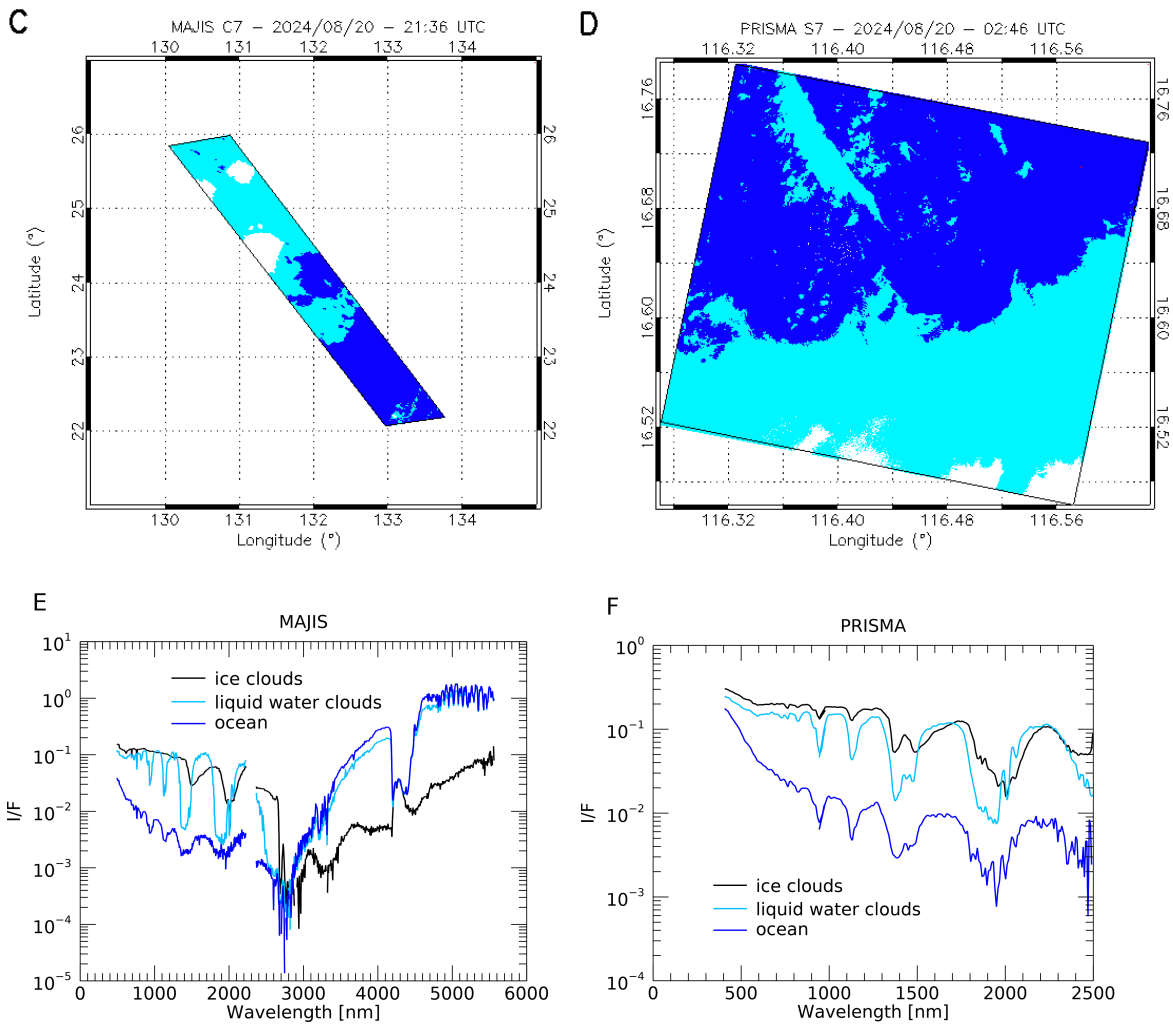
680 4.1. Icy clouds properties

681

682 Examples of two MAJIS and PRISMA cubes containing ice clouds, identified through the ice
683 spectral index in Table 3 (threshold < 1), are given in Figure 11. In the MAJIS case, ice is
684 found in localized convective clouds (Figure 11A and C), so high with respect to the
685 background structures that they even cast well detectable shadows (see Section 4.2.2).
686 Instead, in the PRISMA observation ice is detected both in diffuse bright clouds (e.g. at the
687 southern east corner of Figure 11B and D) and in thinner and less contrasted structures
688 (probably identifiable as high altitude cirrus clouds, e.g. the white regions around longitude
689 116.4° - latitude 16.5° , Figure 11B and D) hence proving the effectiveness of the index with
690 different regimes of ice optical depth. Sample spectra from the identified classes are shown
691 in Figure 11E and F for MAJIS and PRISMA respectively. It must be noted that the very low
692 albedo of the ocean in MAJIS spectrum at visual wavelengths ($< 1\%$) is due to the very slant
693 illumination conditions for the selected observation (incidence angle of about 80° for cube
694 C7, see Table 1). On the other hand, the spectra in the thermal range show consistency with
695 the expected temperature regimes, with very cold ice clouds and the ocean hotter than liquid
696 water clouds.



697



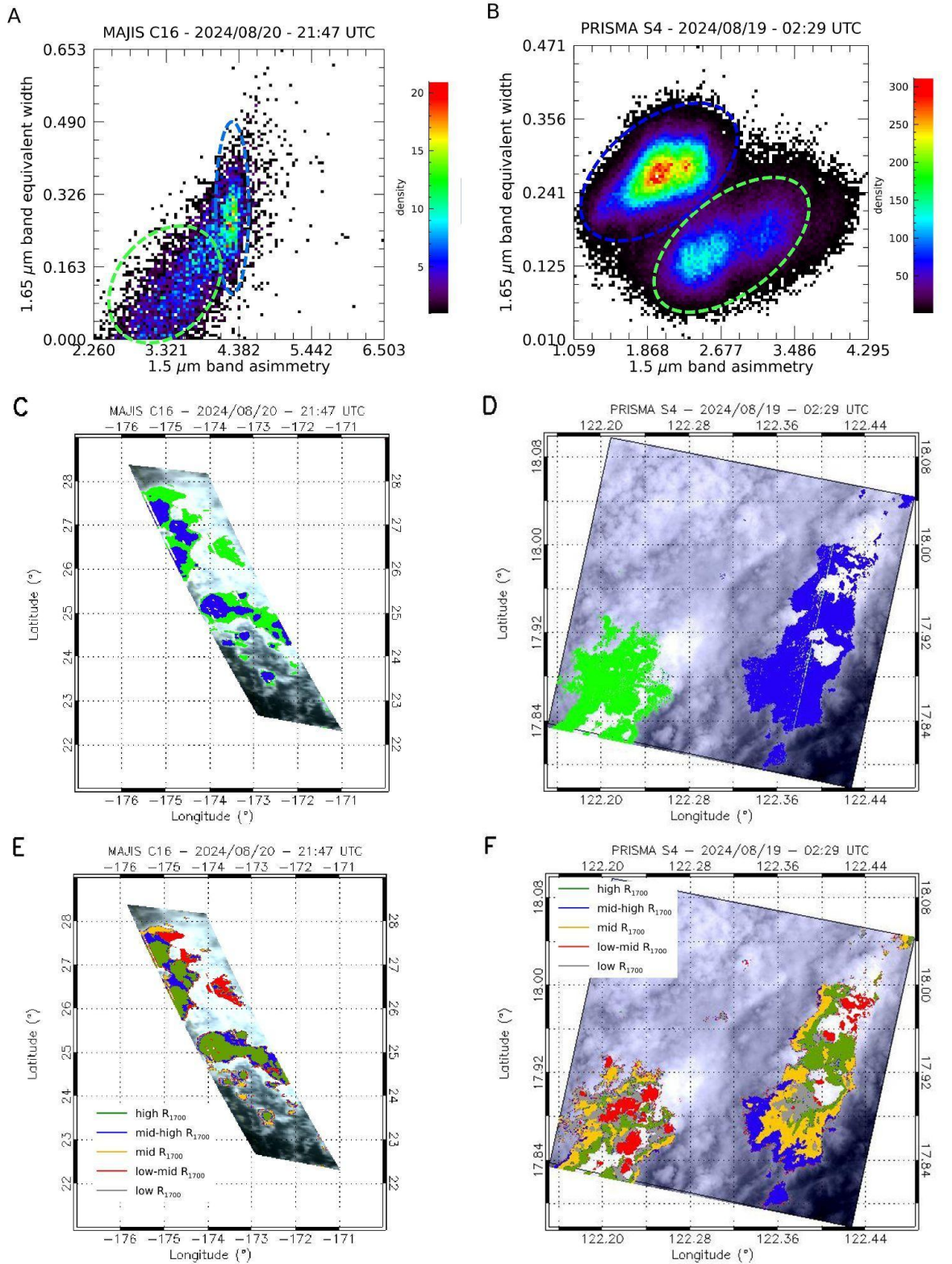
698

699

700 **Figure 11:** Panels **A** and **B** refer to MAJIS cube **C7** and one of the PRISMA cubes from
 701 session **07**, respectively, displayed in RGB. Panels **C** and **D** show the masks for the
 702 detection of ocean (blue), liquid water clouds (cyan, from the “cloudy” condition in Table 3)
 703 and ice clouds (white) pixels related to the two cubes. Panels **E** and **F** display sample
 704 spectra related to the different classes identified in MAJIS and PRISMA observations.

705

706 Ice is similarly widespread in other MAJIS and PRISMA data, so that some considerations
 707 on its distribution and correlations between its parameters can be made (Figure 12). We
 708 compute the 1500 nm band asymmetry as a ratio of slopes, the first considered between
 709 1415 and 1500 nm (left wing) and the second between 1500 and 1790 nm (right wing). The
 710 asymmetry correlates with the strength of the 1650nm band (quantified as equivalent width,
 711 Figure 12A and B), with higher values indicating increasingly crystalline ice (Mastrapa, 2008;
 712 Stephan et al. 2021; Grundy & Schmitt 1998). Different regimes of these two parameters
 713 map localized structures in MAJIS and PRISMA observations, as shown in Figure 12C and D
 714 respectively where green and blue pixels refer to clusters contained within dashed ellipses
 715 sharing the same color in Figure 12A and B. In MAJIS case, the blue cluster is characterized
 716 by an increasing 1650 nm equivalent width at constant 1500 nm band asymmetry. The green
 717 cluster, instead, shows a common trend of growth for the two parameters. On the other
 718 hand, the PRISMA ellipses identify well separated clusters of points within the two
 719 parameters’ space.



720

721

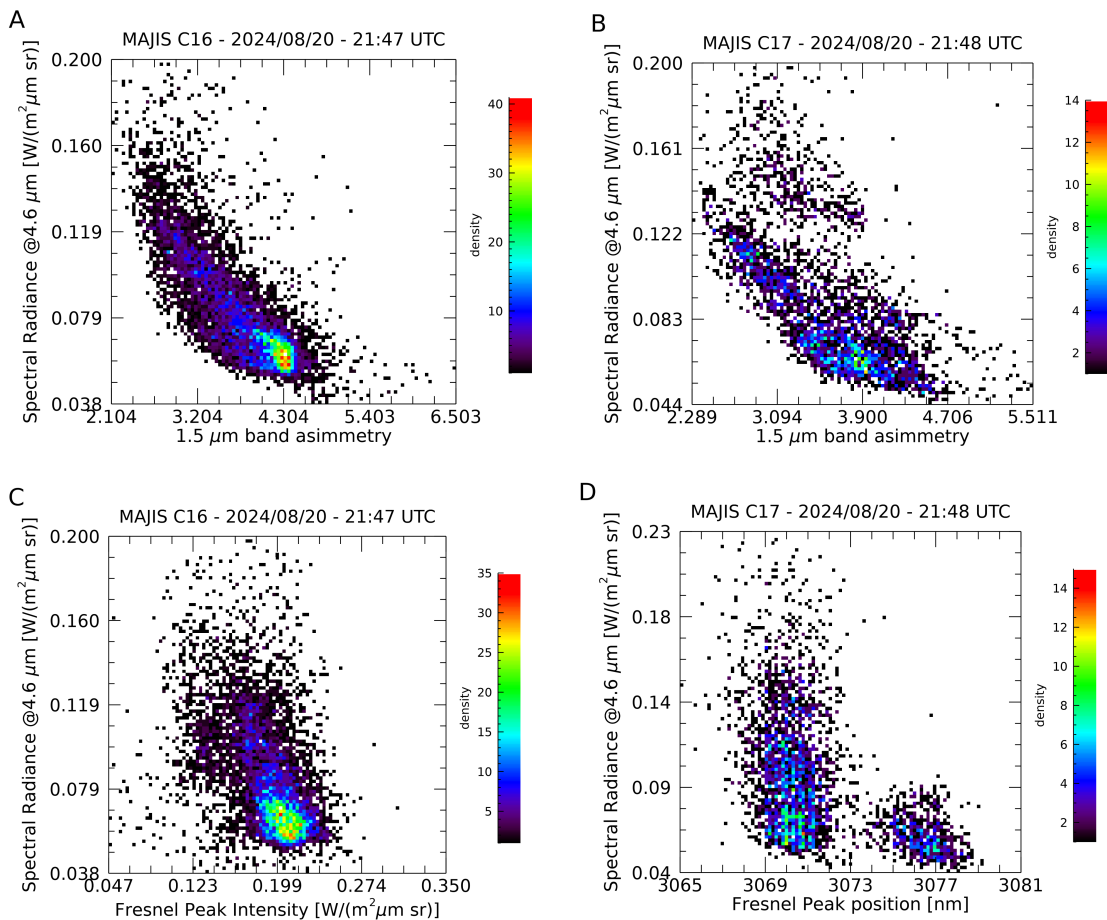
722 Figure 12: **A-B**: scatterplots of the 1500 nm band asymmetry and the 1650 nm band
 723 equivalent width for MAJIS reflectance cube C16 and one of the PRISMA reflectance cubes
 724 from session 04. The colored-dashed ellipses separate different regimes of the two
 725 parameters (see Section 3.5). **C-D**: green and blue pixels map the clusters contained within
 726 the respective ellipses in panels A and B. **E-F**: clustering of ice observations, obtained

727 through the K-means classification algorithm (see Section 3.2), grouped on the basis of the
728 intensity of the reflectance at 1700 nm (R_{1700}).

729

730 It is interesting to note that the correlation between these clusters and those obtained from
731 the K-means classification discussed in Section 3.2 (Figure 12E-F) is not straightforward. For
732 MAJIS, ice spectra with high reflectivity in the solar part of the spectrum (green in Figure
733 12E) are mostly correlated with the blue cluster in Figure 12C. This trend is not observed in
734 PRISMA, where all K-means clusters are equally distributed over both the blue and green
735 clusters shown in Figure 12D, suggesting variable ice densities and grain sizes within the
736 same regimes of crystallinity. This difference derives from the fact that, as explained in
737 Section 3.2, for MAJIS the thermal wavelengths contribute to the K-means classification of
738 the spectra, hence providing information also on the temperature of the ice (see also Section
739 4.2.3). This is verified by the trend of the 1500 nm band asymmetry with the radiance in the
740 thermal part of the spectrum, shown for MAJIS cubes C16 and C17 in Figure 13A-B: more
741 crystalline ice (larger asymmetry) is correlated with lower radiances (i.e. temperatures) at
742 thermal wavelengths. In particular, orbit C17 also shows a detached cluster in the distribution
743 of the thermal radiance suggesting different regimes of temperature (hence different clouds'
744 altitude). Finally, we show the correlation between the ice crystallinity and its temperature in
745 Figure 13C-D, where the intensity and wavelength of the Fresnel peak are compared to
746 MAJIS thermal radiances. Consistently with previous studies (e.g. Stephan et al., 2021), the
747 intensity of Fresnel peak is higher when the temperature is low (Figure 13C), indicating
748 enhanced crystallinity (see also Poulet et al., this issue). The comparison in Figure 13D
749 shows two distinct regimes of the peak position, with the short wavelength cluster
750 characterized by a larger spread of the thermal radiance (suggesting an enhanced
751 temperature variability for a less crystalline ice, e.g. Stephan et al., 2021).

752



753

754

755 **Figure 13: A-B:** scatterplots of the 1500 nm band asymmetry and thermal radiances at 4600
 756 nm for MAJIS orbit C16 and C17 respectively. **C:** scatterplot of the Fresnel peak intensity
 757 with the thermal radiance at 4600 nm for MAJIS orbit C16. **D:** scatterplot of the Fresnel peak
 758 wavelength with the thermal radiance at 4600 nm for MAJIS orbit C17.

759

760 4.2. Clouds' altitude

761

762 We now discuss the altitudes of clouds derived with the different methods presented in
 763 Section 3.3.

764

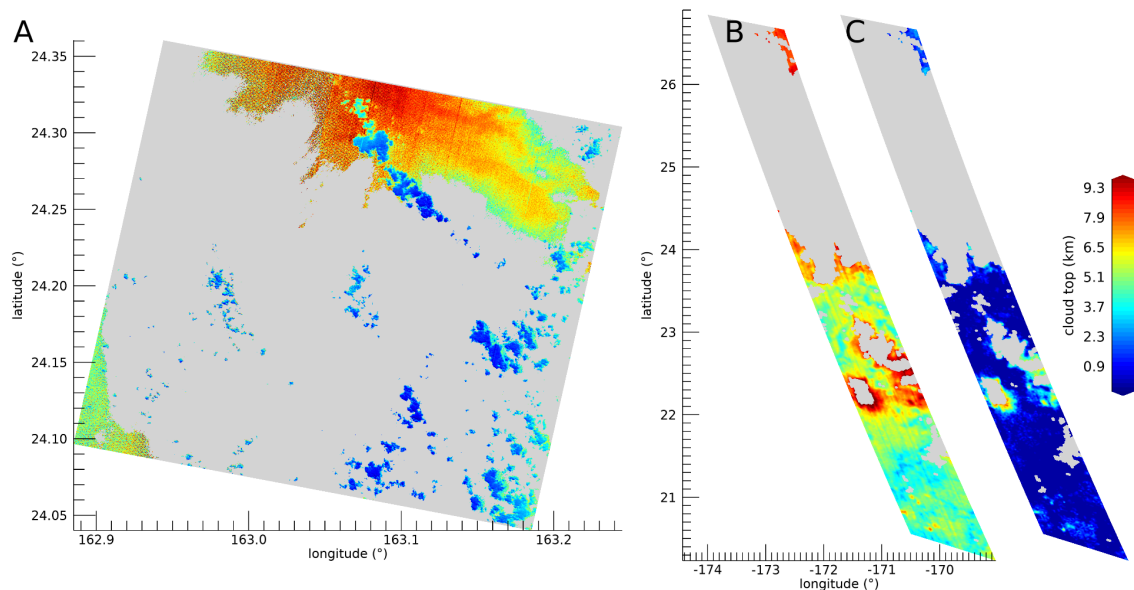
765 4.2.1. Altitudes from O₂ band depths

766

767 Figure 14 shows a comparison of cloud top altitude maps obtained by applying the O₂ bands'
 768 investigation method (Section 3.3.1) to sample PRISMA and MAJIS cubes. In this case,
 769 PRISMA retrievals (Fig.14A) show two main cloud layers, a higher one between 5 and 9 km
 770 (yellow-red colors in the figure, modal value 6.5 ± 1 km) and a lower one between less than 1
 771 and 4 km (blue-cyan colors, modal value 2.0 ± 1 km). MAJIS cloud tops (Fig.14B), whose
 772 model value lies at 4.8 ± 1 km, are in overall agreement with the PRISMA upper cloud deck,
 773 even if the observing angles were very different in the two cases ($>60^\circ$ for MAJIS, $\sim 12^\circ$ for
 774 PRISMA). On the other hand, the population of lower clouds detected by PRISMA appears
 775 broken in a series of localized small structures that could remain unresolved if also present
 776 in the MAJIS scene (see Section 2.3.1). A more systematic discrepancy is obtained when
 777 comparing cloud top altitudes retrieved through the 760 nm and the 1270 nm bands

778 (Fig.14C, shown as reference for MAJIS data only), since the latter gives systematically
 779 lower values (most clouds drop below 1.5 km altitude). This discrepancy reflects the smaller
 780 sensitivity of this band to higher altitudes and the non optimal modeling assumptions
 781 described in Section 3.3.1. However, such an issue can be resolved with a more complete
 782 radiative transfer modeling as suggested by the benchmark presented in Section 4.2.4.
 783

784



785

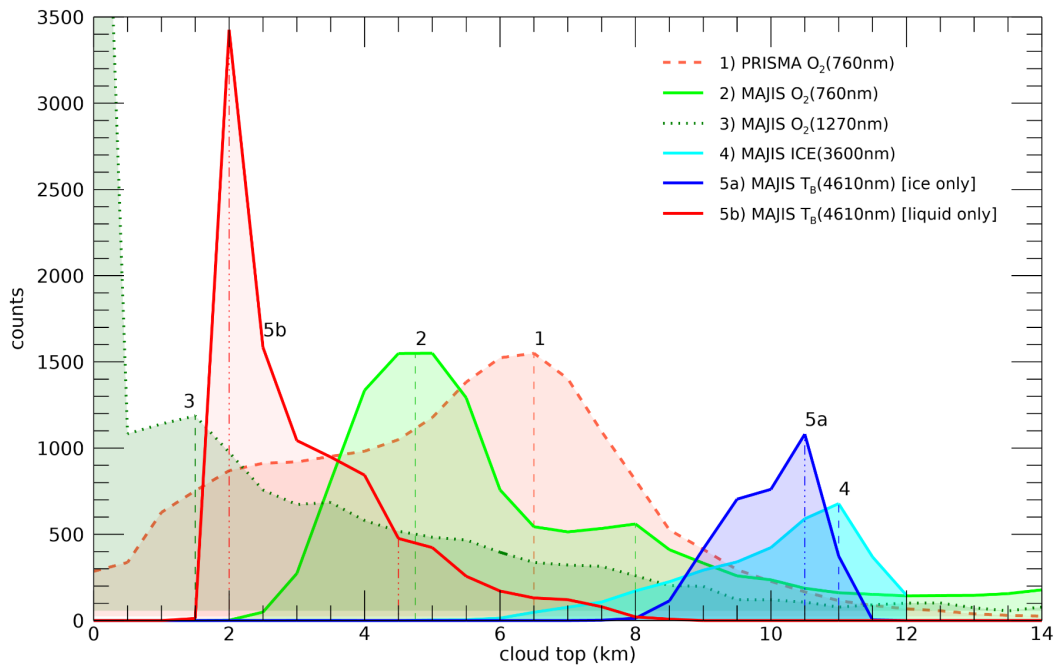
786 Figure 14: **A)** Map of cloud top altitude retrieved through the O₂ 760 nm band in a PRISMA
 787 sequence 09 cube (20240820234657). Non-cloudy pixels or saturated ones, excluded from
 788 the calculation, are shown in grey. **B)** the same as panel A but from a MAJIS data cube
 789 C17. **C)** cloud top map for the same data in panel B (offset for clarity) but retrieved from the
 790 1270 nm O₂ band. Uncertainties are of the order of 1 km (Section 3.3.1).
 791

792

792 The counts distribution of cloud top altitudes derived from the maps in Figure 14 is shown in
 793 Figure 15. The altitude ranges of the main cloud deck derived from the O₂ 760 nm band are
 794 in good overall agreement between MAJIS and PRISMA (light green and dashed light red
 795 curves), characterized by two broad peaks around 4.8 km and 6.5 km, respectively. The
 796 displacement between these peaks is mainly driven by a true difference in the cloud
 797 populations between the two observed scenes, and is further increased by the different
 798 spatial/spectral resolutions. A much lower distribution, flattened towards the surface, is
 799 indicated by the O₂ 1270 nm band, confirming its scarce usability to trace cloud altitudes.
 800 The cloud heights derived from the 3700 nm ice spectral signature (cyan curve) only trace
 801 icy pixels of MAJIS C17 cube (see lower panels of Figure 17) and are distributed, as
 802 expected, above the main cloud deck, with a peak around 11 km. The same behaviour is
 803 also confirmed by the altitudes distribution evaluated through brightness temperatures'
 804 estimation over the same icy spectra (blue curve, 10.5 km peak). The same estimation,
 805 applied to non-icy spectra (red curve), gives altitudes significantly biased toward lower

806 levels. This can be mainly ascribed to the fact that the thermal part of the spectrum of thin
 807 liquid water clouds observations is affected by an enhanced contribution from the ocean
 808 thermal emission. Full radiative transfer calculations would be needed to quantitatively
 809 assess this aspect and the assumptions on the specific emissivity of liquid/ice clouds (set to
 810 1 for both in our calculations), but are not performed here as they are beyond the purpose of
 811 this preliminary work.

812



813

814

815 Figure 15: Comparison of cloud top altitudes retrieved from PRISMA and MAJIS session 09
 816 and C17 cubes respectively, through different methods. PRISMA counts are normalized to
 817 the maximum value of MAJIS curve 2. Distributions derived from O_2 band depths, related to
 818 the maps in Figure 14A, B, C, are shown in pink (dashed line), light green (solid line), and
 819 dark green (dotted line) respectively. Cyan curve refers to ice clouds only (method described
 820 in Section 3.3.3 and discussed in Section 4.2.3), while the distributions obtained from
 821 thermal emission at 4610 nm are given separately for water ice (in blue) and liquid water (in
 822 red) pixels. The heights of the main distribution peaks are highlighted by vertical dashed
 823 lines. Even if the distributions are evaluated in 0.5 km altitude bins, an uncertainty of the
 824 order of 1 km must be considered.

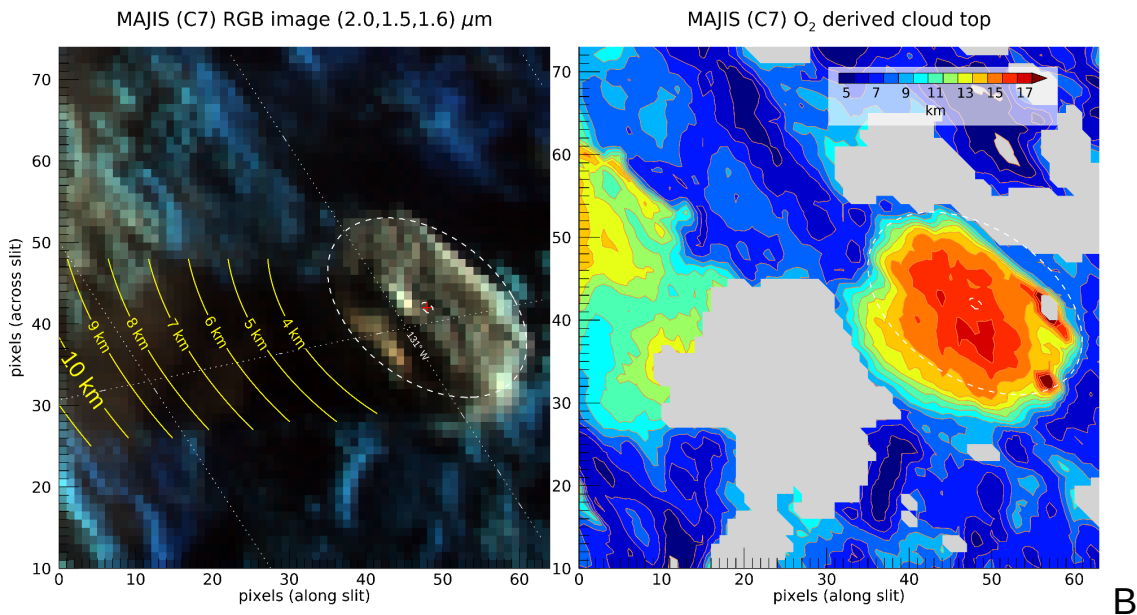
825

826 4.2.2. Altitudes from clouds' shadows

827

828 An example of the results obtained from the method described in Section 3.3.2 is given in
 829 Figure 16, where the shadows projected by high convective anvil clouds are clearly visible in
 830 MAJIS data cube C7. The grazing illumination of the scene (incidence angle $\sim 80^\circ$) enables a
 831 vertical resolution of ~ 0.7 km, inferred from uncertainties of $\sim 0.5^\circ$ on incidence angles and
 832 2.7 km on shadow length (about twice the horizontal spatial resolution). Within this
 833 framework, the horizontal length of the shadow translates to a top altitude of about 10 km

834 (see yellow lines). Of course this value is not absolute but only an estimate relative to the
 835 surrounding decks, whose altitudes can be qualitatively inferred through the estimation of the
 836 O₂ 760 nm band depth (see previous section). The O₂-derived elevations are shown in the
 837 map of Figure 16B, where the background structures appear to be located around 5 - 8 km,
 838 while the anvil cloud top peaks at ~ 16 km. This implies a differential height of ~ 10 km
 839 between the anvil and the surrounding clouds, in very good agreement with the estimated
 840 shadow length. The absolute height of the cloud top can only be derived if multiple scattering
 841 effects are accounted for in the reproduction of the 760 nm O₂ band (Section 4.2.4).
 842 Nevertheless, the shadow analysis provides a quick and independent way for estimating the
 843 relative height of isolated structures with respect to their background.



845 **Figure 16:** A): Example of cloud top altitude estimation based on projected shadow length
 846 in the MAJIS data cube C7. The white dashed line indicates the approximate boundary of a
 847 detached cloud (center indicated by the red dot). The yellow lines show how long the
 848 expected shadow would be in the actual geometry by changing the cloud top altitude. The
 849 shadow length observed in the background image matches a cloud about 10 km tall. B):
 850 Cloud top altitudes retrieved in the same area from the O₂ 760 nm band (see Section 4.2.2),
 851 shown for comparison. Gray-filled patches correspond to areas where no O₂ band is
 852 measurable.

853

854 4.2.3. Altitudes from ice temperature

855

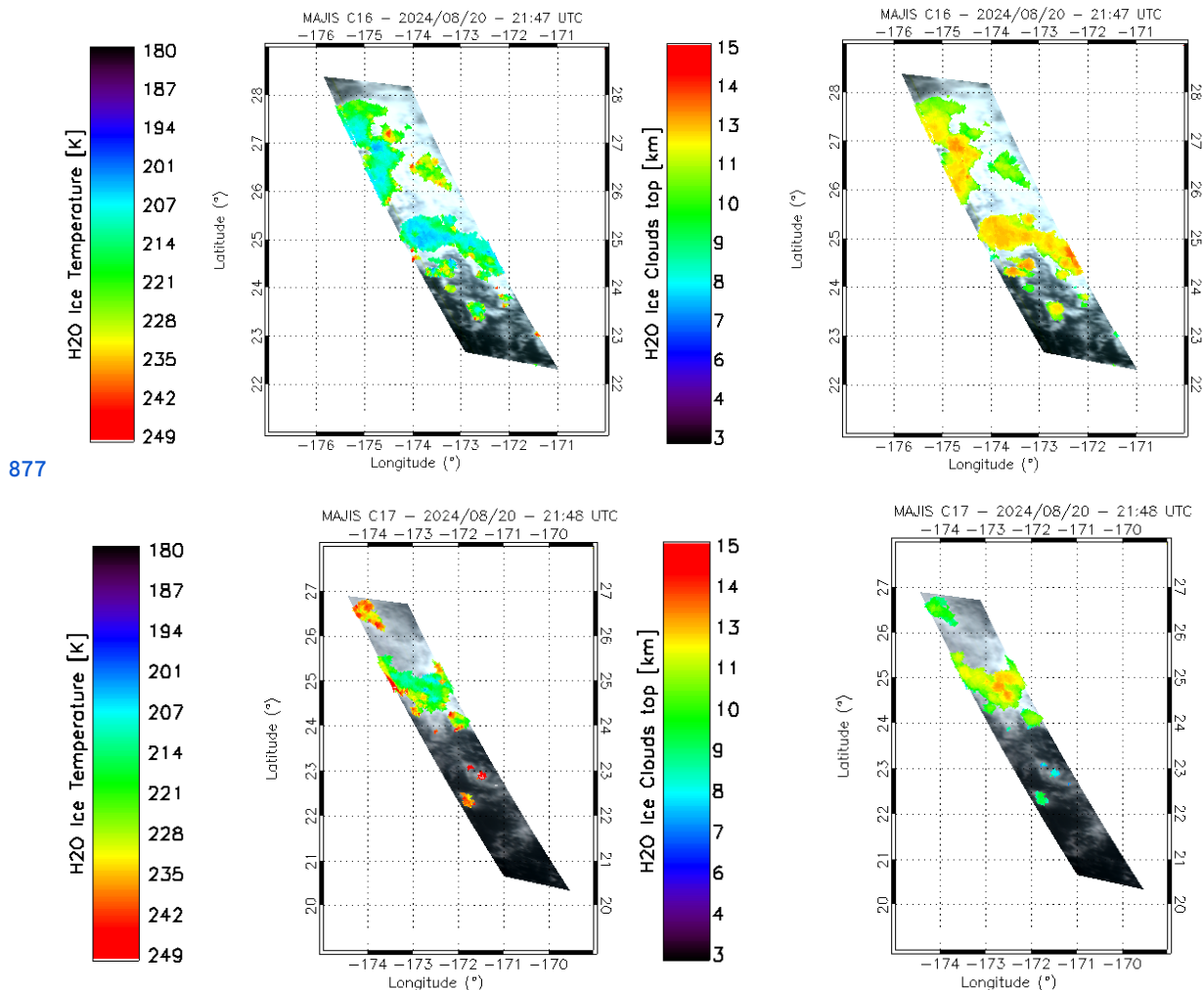
856 In Figure 17 we show two examples of the temperature and altitude maps derived with the
 857 method described in Section 3.3.3, for MAJIS cubes C16 (upper panels) and C17 (lower
 858 panels).

859 Altitudes are derived by assuming that the clouds are in thermal equilibrium with the
 860 surrounding air and reside within the troposphere, where the temperature vertical lapse rate
 861 is positive. Altitudes' errors are of about 1 km (Section 3.3.1) while those related to
 862 temperatures are propagated from the 3700 nm peak uncertainties (Table 4) and result of
 863 about 1 K. Orbit C16 shows two main decks, placed respectively at $z \sim 13$ km and $z \sim 10$ km
 864 which can be compared with the maps in Figure 12C and E, where the 1650 nm band depth
 865 and K-means clusters are shown. The higher deck at $z \sim 13$ km correlates with the blue

866 cluster in Figure 12C and the green one in Figure 12E, suggesting increased opacity and
 867 crystallinity at lower temperatures.

868 Similarly, two regimes of temperatures and altitudes are found in orbit C17, with higher
 869 clouds at $z \sim 13$ km ($T \sim 205$ K) and lower ones at $8 < z < 10$ km ($215 < T < 250$ K). As
 870 suggested by the scatterplot in Figure 13D, these two decks are characterized by different
 871 ice properties. Indeed, the short wavelength Fresnel peak cluster (i.e. reduced crystallinity,
 872 Cartwright et al., 2025) shows a larger spread of temperatures, consistent with the lower
 873 clouds discussed here. Instead, the long wavelength Fresnel peak cluster shows overall
 874 lower thermal radiances, and hence temperatures, in agreement with the higher clouds
 875 identified at ~ 13 km (see also Poulet et al., this issue).

876



877

878

879 **Figure 17:** ice temperature (left) and inferred cloud altitude (right) mapped on MAJIS cube
 880 C16 (upper panels) and C17 (lower panels). Ice is identified with a threshold < 1 on the ice
 881 clouds condition in Table 3.

882

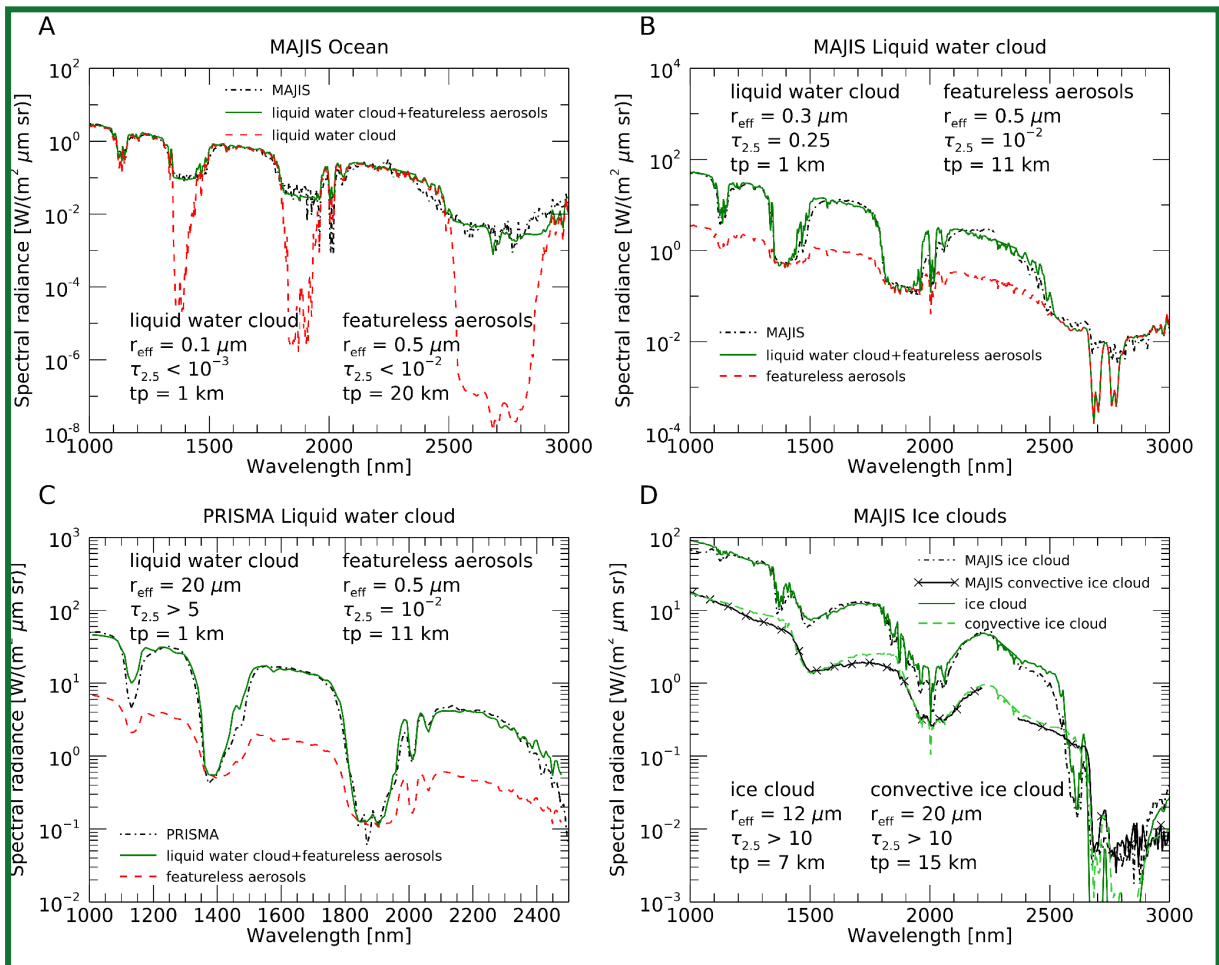
883

4.2.4. Results from RT modeling

884

885 For our forward RT modeling (Section 3.3.4) we consider all MAJIS spectra and the PRISMA
 886 liquid water cloud one from Figure 3, as it is the one showing the most evident differences
 887 with respect to its MAJIS counterpart. We also take into account a MAJIS ice cloud spectrum

888 related to one of the convective structures identified in Figure 11A-C and studied in Section
 889 4.2.2.
 890



891
 892 **Figure 18:** Panel A: MAJIS ocean spectrum from Figure 3 is shown in dashed-dot black, its
 893 forward RT fit is shown in green, while the contribution from the liquid water cloud in the
 894 simulation is given in dashed red. Geometrical and microphysical parameters (r_{eff} is the
 895 effective radius in μm , $\tau_{2.5}$ is the optical depth at $2.5 \mu\text{m}$ and tp is the cloud top in km) of
 896 aerosols involved in the fit are given in the figure. Panels B-C: same as in panel A, but liquid
 897 water clouds observations by MAJIS and PRISMA from Figure 3 are respectively fit. The
 898 dashed red lines here refer to the contribution from the featureless aerosols in the model (i.e.
 899 when no liquid water cloud is considered). D: MAJIS ice clouds forward RT fits (green and
 900 dashed light green lines) related to MAJIS ice cloud spectrum from Figure 3 (dashed-dot
 901 black) and to a spectrum from the convective cloud identified in Figure 11C (black line
 902 with crosses).

903
 904 The best fits obtained with this approach are shown in Figure 18. In general, grain sizes and
 905 clouds' altitudes determine the shape and the signal of water absorption bands, while the
 906 number density can be tweaked to match the intensity of the continuum. We assume that the
 907 clouds are compact in vertical extent and only occupy a single layer of the atmospheric
 908 profile. The ocean and liquid water clouds observations require two separate layers placed
 909 at different altitudes in the atmosphere (Figure 18A, B and C) suggesting that, as explained
 910 in Sections 2.3.1 and 3.1, also the ocean spectra we are investigating are partially
 911 obstructed by non-resolved cloudy structures. The lower layer shapes the shoulders of water

bands', in which the atmospheric transmission is enough to probe down to the surface, while the upper one is needed to correctly model the intensity of the bands' bottom. Indeed, if optically thick enough, high clouds prevent solar photons from reaching the underneath atmospheric layers, hence reducing the gaseous absorption. Such a differential effect in the models is shown as dashed red lines in Figure 18A, B, C. In the ocean spectrum (Figure 18A) the optically thin bottom layer ($z = 1$ km, $\tau < 10^{-3}$) with small grain sizes ($r_{\text{eff}} = 0.1$ μm) is consistent with the average properties of maritime droplets ($0 < z < 2$ km, $5 \times 10^{-4} < \tau < 10^{-3}$, $0.05 < r_{\text{eff}} < 1.5$ μm) commonly observed above the surface of the ocean (Croft et al., 2021; Smirnov et al., 2002; Heintzenberg et al., 2000). On the other hand, the upper thin layer ($\tau < 10^{-2}$) has slightly larger particles ($r_{\text{eff}} = 0.5$ μm) and is placed at 20 km, in agreement with the presence of stratospheric background aerosols ($15 < z < 25$ km, $10^{-4} < \tau < 10^{-3}$, $0.1 < r_{\text{eff}} < 1$ μm , Voudouri et al., 2023; Thomason et al., 2008). Such a configuration confirms the observation as a partially obstructed scenario.

The selected MAJIS and PRISMA liquid water clouds observations (Figure 3 and Figure 18B-C) show a good radiometric agreement but differences in water bands' shape that can be explained by changes in the aerosols' microphysical properties. Both observations are characterized by a high altitude, spectrally featureless, thin aerosol layer ($z = 11$ km, $\tau \sim 10^{-2}$) that is required to reproduce the bottom of water bands. This indicates the presence of faint background stratospheric aerosols residing at the tropopause. Instead, the lower liquid water layer ($z = 1$ km) is thin with small grains in the MAJIS case ($\tau = 0.25$, $r_{\text{eff}} = 0.3$ μm) suggesting spray marine boundary layer aerosols (Sun et al., 2023; Zheng et al., 2018; Luo et al., 2014), and thicker with large grains in the PRISMA case ($\tau > 5$, $r_{\text{eff}} = 20$ μm), consistent with the presence of stratus clouds (Fu et al., 2022; Rossow and Shiffer, 1999; LeMone, 1988). Hence, different properties ensure the modeling of flatter (MAJIS) and sharper (PRISMA) bands in the two observations.

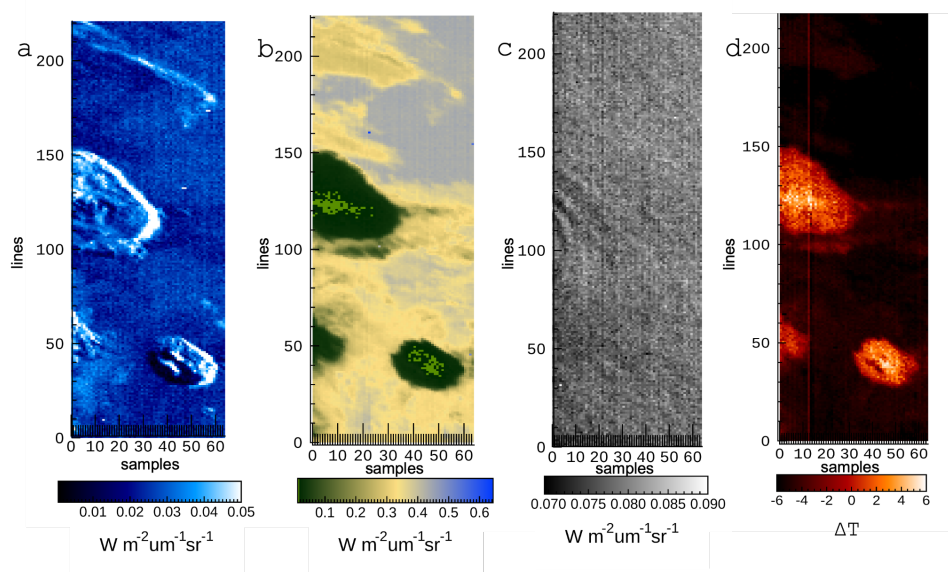
The two ice observations (Figure 18D) are reproduced with a single cloud layer and do not require the lower one. This is because the ice clouds in the models have opacities so high ($\tau > 10$) that they prevent observing the ocean and the atmospheric layers in between. In such conditions, the ice cloud in practice acts as a surface with high albedo, accounting for most of the spectral features in the observations. However, two different clouds' observations are considered here. The first one (black dashed-dot line in Figure 18D) is related to a small structure identified around longitude 133° and latitude 22° in Figure 11C. This cloud can be modelled with ice crystals of the order of 10 μm in radius (green line). The altitude can be reliably tweaked by studying the depth of gaseous water absorption bands at 1380 nm and 2600 nm, both identifiable in the observation. This means that the ice cloud is low enough to ensure some water absorption, before completely shielding the underneath atmosphere. As a result, our estimate is that it has its top at 7 km. These parameters suggest compatibility with the presence of a thick cirrus cloud ($6 < z < 13$ km, $\tau > 3$, $10 < r_{\text{eff}} < 60$ μm , Baran, 2009; Zhou et al., 2017; LeMone, 1988).

The other ice cloud (black blue line with crosses in Figure 18D) is selected on the larger convective structure identified in Figure 11C. We already expect this to be higher in the atmosphere with respect to the other one (Section 4.2.2). Our model (dashed light green-red line) suggests that it is characterized by larger crystals (20 μm) and reaches an altitude of at least 15 km, enough to prevent water absorption in the 1380 and 2600 nm bands (the model sensitivity to higher altitudes is reduced making this estimate a lower limit). These values indicate that in this observation MAJIS is probing the upper frozen top of a large convective cloud ($8 < z < 16$ km, $\tau > 10$, $10 < r_{\text{eff}} < 60$ μm , Dolan et al., 2023; Krisna et al., 2018; van Dienenhoven et al., 2018).

960
961
962
963
964
965
966
967
968
969
970
971
972
973
974
975
976
977
978
979

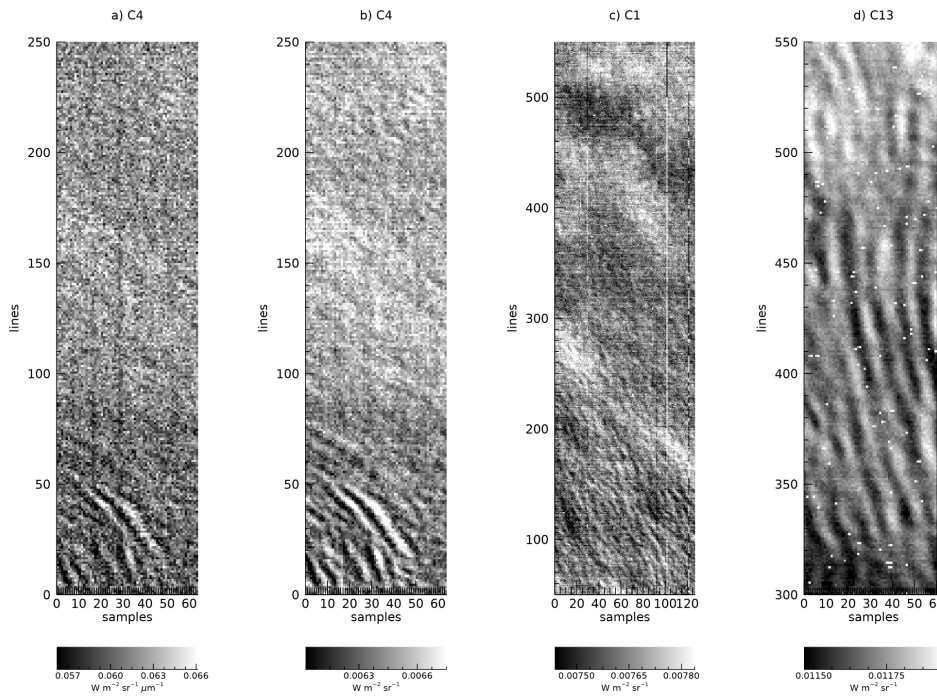
4.3. Upper atmosphere features

The CO₂ and O₃ emissions introduced in Section 3.4 have been studied in all MAJIS cubes, deriving maps like those shown in the examples of Figure 19 and Figure 20. In Figure 19, panels A and B show MAJIS cube C7 displayed at 3100 and 4512 nm, whose anti-correlation highlights the presence of the convective clouds discussed in Sections 4.1, 4.2.2 and 4.2.4. Panels C and D, instead, show the radiance of the peak of CO₂ emission at 4270 nm and the brightness temperature difference between the O₃ emission peak and its continuum (Section 3.4). It is evident how wavy patterns can be seen in the CO₂ map and are uncorrelated with the clouds beneath. No wave patterns are spotted from the O₃ emission, whose positive values (and hence the emission) are only detectable above the convective structures. This suggests that, while both phenomena are likely happening above the clouds' top, waves are generated at different altitudes with respect to those pertaining to the O₃ emission. However, the actual heights are not investigated here, since a rigorous retrieval accounting for non-LTE effects (required for the assessment of these high-altitude emissions) is beyond the scope of the paper.



980
981
982
983
984
985
986
987
988
989
990
991

Figure 19. A-B: MAJIS cube C7 radiances at 3100 nm and 4512 nm respectively, highlighting the anti-correlation between enhanced ice content (A, i.e. larger reflectances of the Fresnel peak) and low thermal contribution (B). C: radiance of the CO₂ emission peak at 4270 nm, in which the gravity wave pattern is identified. D: brightness temperature difference (in K) between the O₃ emission peak (4717 nm) and its continuum (4660 nm), showing positive values above the clouds. In all maps, 'samples' and "lines" indicate spatial pixel numbers in the direction along and across the instrument slit respectively.



992

993 **Figure 20.** A circular wave pattern is clearly observed in MAJIS C4 cube at 4270 nm (panel
 994 a). Panel b shows the enhanced contrast achievable after spectral integration between 4254
 995 and 4333 nm, which also improves detection of complex wave patterns in several MAJIS
 996 observations, like in C1 (panel c) and C13 (panel d). Pixel scales are reported in Table 1.

997

998 Following the discussion in Section 3.4, in Figure 20 we show the effect of the increased
 999 contrast that can be achieved through the spectral integration of the CO₂ emission (right
 1000 panel), with respect to the single wavelength investigation (left panel). The integration
 1001 reduces noise hence allowing enhanced accuracy in detecting the wave patterns. Indeed, if
 1002 the radiance integrated in the band is considered, the detectable relative intensity drops from
 1003 1% to about 0.5%, which translates as an increased capability in characterizing the vertical
 1004 structure of the waves.

1005

1006 4.3.1. Atmospheric waves properties

1007

1008 Examples of wavy structures identified in the MAJIS images at 4270 nm are provided in
 1009 Figure 20. The wave packets have characteristics different from one image to the other in
 1010 terms of orientations and horizontal wavelengths. In some cases, a curved wavefront is
 1011 observed (see Figure 20 B, C, D) as well as a superposition between different packets
 1012 (Figure 20 D).

1013

1014

| ID | Latitude (deg) | Packet length (km) | Packet width (km) | Horizontal wvl (km) | Azimuth (deg) |
|----|----------------|--------------------|-------------------|---------------------|---------------|
| C1 | 9-10 | 157.6 | 36.1 | 27±7 | 163 |
| C2 | 10-14 | 155 | 135.2 | 20±6 | 160 |
| C4 | 20.85 | 107.9 | 94.7 | 21±6 | 162 |

| | | | | | |
|-----|-----------|-------|-------|-------|------|
| C5 | 17.7-18.4 | 154.1 | 159.1 | 16±5 | 33.5 |
| C6 | 22.9 | 74.5 | 94.8 | | 133 |
| C7 | 23.4-25.5 | 84.5 | 73.8 | 15±6 | 155 |
| C13 | 19-22 | 134.6 | 88.1 | 24±8 | 123 |
| C16 | 25-27 | 174.5 | 131 | 28±11 | 119 |

1015 **Table 5:** Summary of atmospheric waves parameters (packet length and width, horizontal wavelength
1016 and azimuth) calculated from MAJIS data analysis. Columns indicate: image cube, latitude (deg),
1017 packet length (km), packet width (km), horizontal wavelength (km), azimuth (deg, see Section 3.4.1),
1018 respectively.

1019

1020 The values obtained from the method described in Section 3.4.1 are provided in Table 5. In
1021 the observed waves, the measured wavelengths are in the range ~ 15-40 km, which can be
1022 considered as short wavelengths. Similar waves can be generated by several sources and
1023 are usually observed in the stratosphere. According to models, deep convection is the
1024 principal source of forcing (Fovell et al. 1992; Piani et al. 2000; Lane et al. 2001) and is also
1025 suggested to be responsible for circular wave fronts (alongside isolated thunderstorm
1026 events, e.g. as observed from the Midcourse Space Experiment, Dewan et al. 1998).
1027 Another source of gravity waves, related to wind flow over mountains, is orography (Fritts
1028 and Alexander 2003; Kim et al. 2003). Depending on the topography, this can generate
1029 waves with horizontal scales from a few to hundreds of kilometers (Nastrom and Fritts, 1992;
1030 Dornbrack et al. 2002; Eckermann et al. 2007). However, as the majority of MAJIS EGA
1031 observations occurred above open sea areas, a possible origin related to a thunderstorm
1032 seems to be more realistic.

1033 For circular waves, we estimate the packets' properties and the time of occurrence of the
1034 related thunderstorms (see Section 3.4.1). We assume storms occurring at an altitude of 15
1035 km (from thermal brightness estimations) and consider cubes C7 and C4 as examples. The
1036 minimum and maximum radii, along with the expansion speed and wavelength derived from
1037 the images, are as follows: for cube C7, these parameters are respectively 35 km, 50 km,
1038 about 45 km/h and 15 km; for cube C4 they are 20 km, 110 km, about 100 km/h and 20 km.
1039 In both cases, the thunderstorm-triggering events appear to occur approximately one hour
1040 before the corresponding observations. This is compatible with the NASA Worldview archive,
1041 where several thunderstorms have been registered over the areas observed by MAJIS at
1042 around 05:00 local time. In particular, the wave detection in MAJIS C4 acquisition is located
1043 about 80 km far from the coastline, and no significant orographic features are present along
1044 the apparent direction of propagation. For this detection, the hypothesis of
1045 thunderstorm-generated waves is also strengthened by the intense electrical activity
1046 confirmed in D'Aversa et al. (this issue), where a lightning event has been detected in the
1047 visible range of MAJIS cube C1 through the identification of neutral atomic oxygen and
1048 nitrogen emission lines.

1049

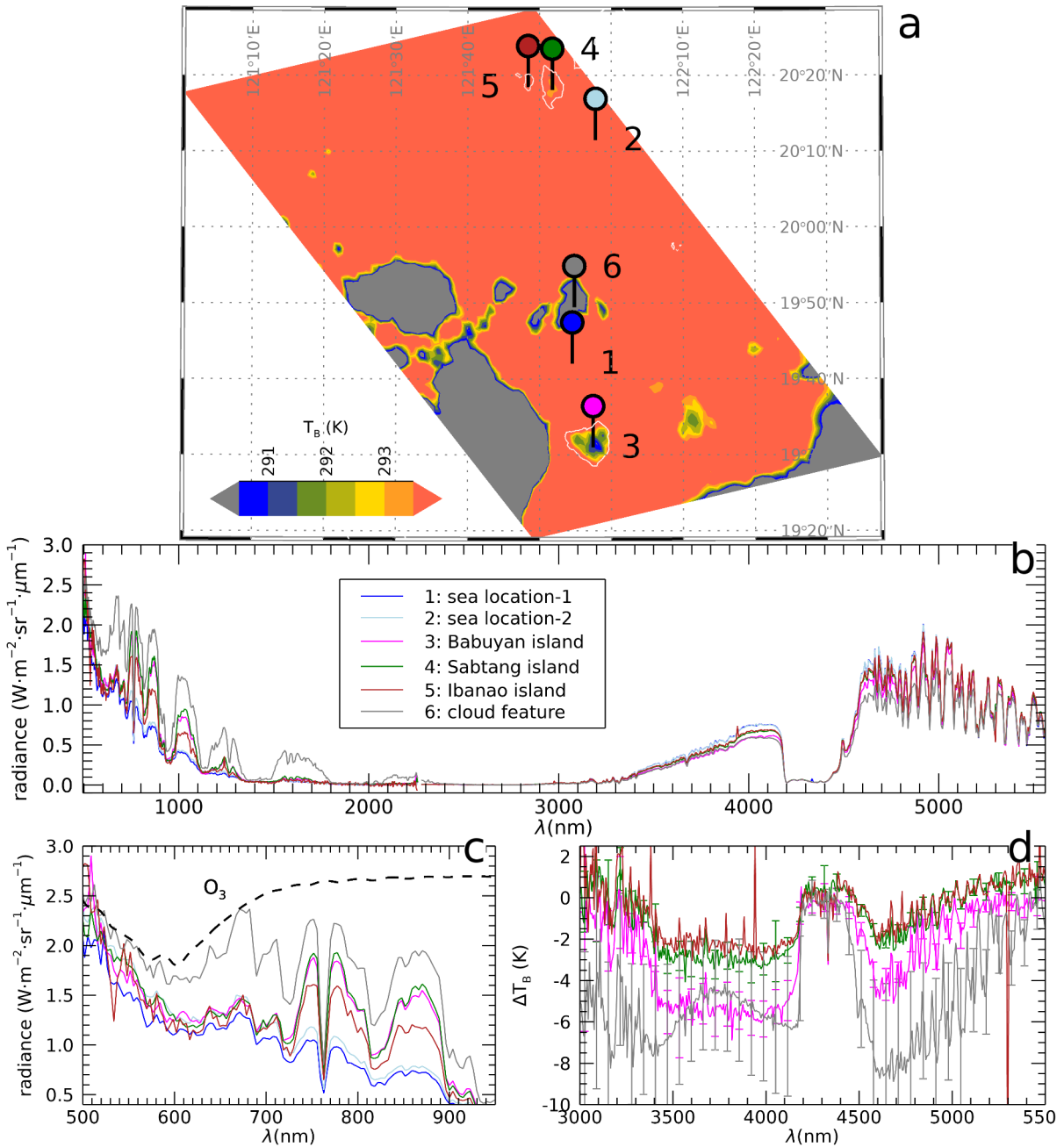
1050 **4.4. Land features**

1051

1052 The land/ocean-contrast detection method described in Section 3.1 has been applied to all
1053 MAJIS cubes, but only a few land features have been identified. The C1 and C2 cubes,
1054 expected to cover large land areas at nighttime, encountered very thick and extended storm

1055 systems that prevented any surface visibility. Hence, all observable land regions consist of
 1056 small islands seen in twilight illumination, colder than the surrounding sea surface but barely
 1057 observable at visible wavelengths. Besides the largest example (Figure 7), other islands are
 1058 found in the cube C5 (Figure 21): Babuyan (region 3), Sabtang (region 4), and the very small
 1059 Ibahos island (about 4 x 2.5 km wide, region 5), all part of the Batanes archipelago. The
 1060 nearby Dequey island, even smaller (~0.7x1 km), remains unresolved. With respect to the
 1061 ocean, the brightness temperatures measured over land and cloud areas (Figure 21b) are
 1062 colder, with differences up to ~6 K and ~8 K respectively. Even if fully located beyond the
 1063 terminator (solar incidence angle ~90.8°), a significant signal is detectable also at visible
 1064 wavelengths, ascribable to light scattering in the upper illuminated portion of the atmospheric
 1065 column, and to multiple scattering effects in the lower part.

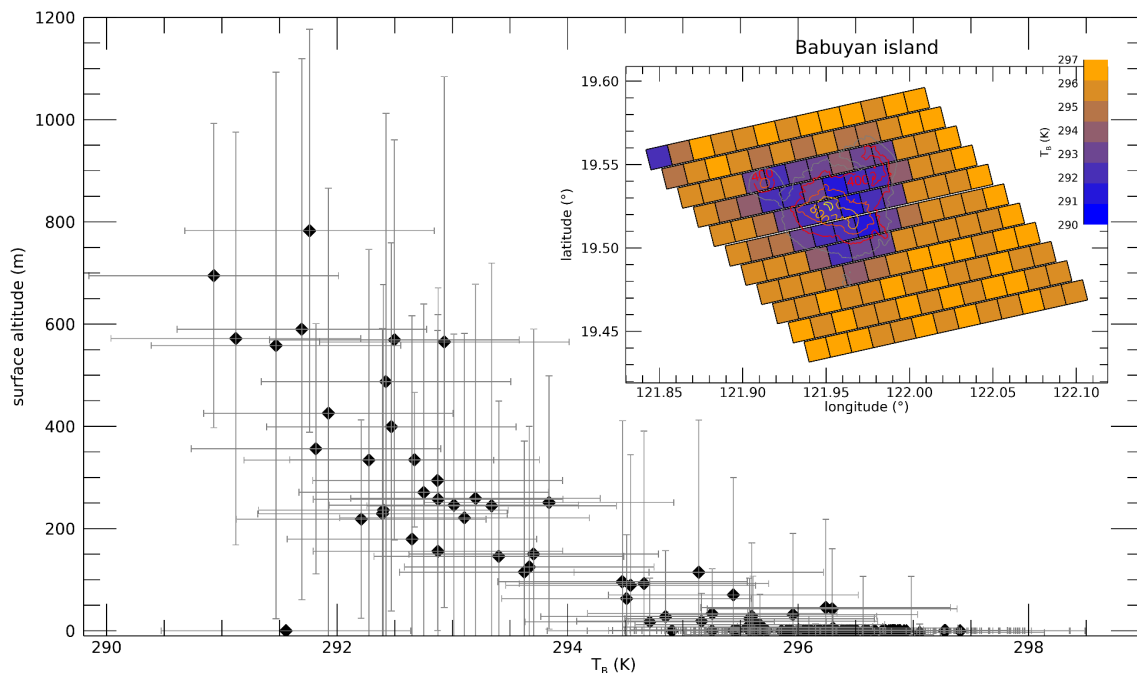
1066



1067

1068 Figure 21: Land spectral features seen in twilight conditions in MAJIS cube C5. **a)** Regions of
 1069 interest (ROIs, labeled 1 to 6) are selected over a 4610 nm brightness temperature map. The
 1070 coldest areas (in gray) are identifiable as thick clouds, while land areas are slightly warmer
 1071 (islands of Babuyan, Sabtang and Ibahos, regions 3, 4, 5 respectively), but still colder than
 1072 the surrounding ocean (red-orange area). Coastlines, obtained from OpenStreetMap under
 1073 the Open Database License, are shown as white lines. **b)** MAJIS full-range spectra over the
 1074 ROIs. **c)** Blow-up of the visible spectral part, showing H₂O and O₂ absorption bands as well
 1075 as a broad O₃ absorption (see also Figure 4). **d)** Blow-up of the infrared spectral part given
 1076 as T_B difference with respect to the ocean spectrum.
 1077

1078 The MAJIS sensitivity to temperature variations can be estimated from the signal fluctuations
 1079 over cloud-free ocean regions. The resulting uncertainties in thermal brightness (at 4610 nm)
 1080 vary between 0.5 and 1 K, which correspond to about 0.2% and 0.4% of the radiance at
 1081 293K. This sensitivity appears sufficient to discriminate significant temperature variation not
 1082 only between sea and land surfaces but also between different land regions. As an example,
 1083 we show in Figure 22 the variability of MAJIS brightness temperature inside the Babuyan
 1084 island, which hosts a volcano of about 1 km in elevation (Babuyan Claro Volcano). Even if
 1085 the spatial resolution is limited, a clear trend emerges with respect to the topographic
 1086 altitude, suggesting that the MAJIS data are sensitive to the surface altimetric temperature
 1087 change.



1088
 1089 **Figure 22:** Thermal analysis of Babuyan island, as viewed in MAJIS data cube C5. The
 1090 MAJIS-derived brightness temperature (at 4610 nm) is plotted against topographic altitude,
 1091 stressing the detection of surface altimetric temperature change. Error bars on the x axis
 1092 derived from signal fluctuation over sea surface around the island, while those on y axis
 1093 represent the variability of surface altitude inside individual MAJIS pixels. Unit emissivity has
 1094 been assumed everywhere. Topographic data are extracted from Google Earth Pro
 1095 7.3.6.10441 (accessed September, 03, 2025).
 1096

1097 **5. Application to Jovian system science**

1098

1099 This flyby represents the first acquisition of planetary data by MAJIS. Although the analysis
1100 presented here has been dedicated to Earth science, we can briefly identify and discuss
1101 different links to the MAJIS science that is foreseen at Jupiter and its icy satellites,
1102 highlighting the instrument capabilities in exploring different objects of the solar system.

1103

1104 **5.1. From ice clouds to icy surfaces**

1105

1106 The detection of terrestrial ice clouds described in Section 4.1 represents the first spectral
1107 observations of water ice performed by MAJIS, and is therefore the first approach to
1108 establish the potential outcomes from observations of Jovian icy satellites, in particular for
1109 Callisto and Ganymede.

1110 The investigation of ice properties possibly provides information on the differential evolution
1111 these bodies underwent in the Jovian system environment. For example, Callisto's surface is
1112 mainly covered by crystalline ice, while significant amorphous ice patches have been
1113 observed on Ganymede (e.g. Tosi et al., 2024, Bockelée-Morvan et al., 2024; Cartwright et
1114 al., 2024). These regions could indicate alteration through radiolysis induced by the
1115 impinging of charged particles on the ice (Khurana et al., 2007), hence providing information
1116 on the mechanisms connecting Jupiter's magnetic field lines and the moons' surfaces.
1117 Moreover, while Callisto is characterized by an overall low ice content on the surface (~
1118 50%) and presents a more ancient and stable scenario (Greeley et al., 2007), Ganymede's
1119 fresh ice patches are indicative of more frequent ice resurfacing and cryo-volcanism events
1120 (Ligier et al., 2019). Smaller ice crystals are observed at the poles, matching the distribution
1121 of the fresher ice deposits and hence acting as a tracer of geologic activity. In this view, the
1122 investigation of ice-related spectral parameters can be used to address many scientific goals
1123 of the JUICE mission (Stephan et al., 2021a; Poulet et al., 2024a).

1124

1125 **5.2. Clouds**

1126

1127 Jupiter's atmosphere is thought to be dominated by the presence of three main cloud decks
1128 residing at different altitudes and mixed by convective processes and atmospheric circulation
1129 (Fletcher et al., 2023). From lower to higher heights these are respectively composed of a
1130 H₂O-NH₃ liquid solution, NH₄SH solid aggregates, and NH₃ ice crystals (Atreya et al., 1999).
1131 In particular, the NH₄SH and NH₃ clouds can be responsible for the chromatic differences in
1132 Jupiter's dark "belts" and bright "zones". Above these structures, hazes composed of
1133 products of the photochemical disruption of CH₄ and NH₃ extend from the upper troposphere
1134 to the stratosphere (e.g. Sindoni et al., 2017; Biagiotti et al., 2025). Such cloud complexity is
1135 not present in Earth's atmosphere where water is the only condensible, aside from a variety
1136 of aerosols of different origin (e.g. maritime, volcanic, smog, stratospheric). Nevertheless,
1137 the study of EGA observations allows a first MAJIS data analysis devoted to disentangling
1138 the spectral information related to different sources, like gases, clouds and, in this case, also
1139 surfaces. In this manuscript we have investigated clouds under different points of view,
1140 including their detection, water vapour phase identification, vertical structure assessment,
1141 and microphysical properties estimation. All these techniques are applicable to Jupiter once
1142 adapted to the different composition and structure of the giant planet. For example, the RT
1143 modeling presented in Section 4.2.4 only dealt with the solar part of the spectrum, which
1144 would only allow the investigation of Jupiter's hazes and the NH₃ deck (e.g. the recent work
1145 of Biagiotti et al., 2025 on JUNO/Jiram data). The exploitation of the full MAJIS spectral

1146 range, including thermal wavelengths, is instead mandatory for characterizing the deeper
1147 NH_4SH (Grassi et al., 2021) and H_2O (Bjoraker et al., 2022) clouds, especially in “hot spot”
1148 regions.

1149 The shadow technique for measuring cloud heights, commonly applied in planetary
1150 high-resolution imaging analysis, is also applicable to Jupiter (e.g. Orton et al., 2017). For
1151 instance, in observations acquired at the bottom of methane bands, Simon et al. (2015) were
1152 able to measure shadows 45 km long, revealing wavy structures less than 1 km in amplitude.
1153 In principle, MAJIS observations of Jupiter atmosphere will allow the application of this
1154 technique to limited cases, mostly near the terminator and in polar regions when observed
1155 from perijove. Maximum spatial resolutions of ~ 120 km/px achievable in these conditions
1156 may enable detecting shadows related to vertical displacements of the order of 10 km.

1157

1158

1159 **5.3. High-altitude emissions**

1160

1161 The use of chemical atmospheric species as tracers for the atmospheric circulation,
1162 including wind measurements and wave detections, is widely applied to the investigation of
1163 both terrestrial (i.e. Hueso et al. 2008; Peralta et al. 2008) and giant planets (i.e.
1164 Müller-Wodarg et al. 2019, Grassi et al., 2020). A similar approach is valid for the upcoming
1165 MAJIS measurements at the Jovian system, whose upper atmospheric dynamical structure
1166 can be investigated through the monitoring of the distribution (in latitude and local time) of
1167 minor widespread species like H_3^+ and hydrocarbons deriving from the photolysis of methane
1168 (see Miller et al. 2020 for a thorough review) as demonstrated from both ground-based (see
1169 for example O’Donoghue et al. 2016) and space-based data analyses (e.g. Moriconi et al.
1170 2020). MAJIS IR channel will allow to spectrally discriminate the CH_4 and H_3^+ contributions in
1171 the range 3000 - 4000 nm, where the two species present strong features (Castagnoli et al.,
1172 2025) identifiable within the fundamental 3300 nm CH_4 absorption band, similarly to the case
1173 of the 4300 nm CO_2 band in Earth’s atmosphere (see Section 4.3). The study of CH_4 and H_3^+
1174 (e.g. JWST data analysis, Melin et al., 2024) will give access to upper atmospheric layers
1175 which are hardly probed otherwise. Altitudes from about 200 km above the 1-bar level are
1176 typical of methane emission peak, while above 500 km the H_3^+ emission seems to dominate,
1177 as also shown by recent analyses of JIRAM-Juno data (Migliorini et al. 2023), where the two
1178 species have been spatially separated.

1179

1180 **6. Summary and conclusions**

1181

1182 In this work we compare the observations of the MAJIS spectrometer on board the JUICE
1183 spacecraft, acquired during the Earth gravity assist of 2024 (Section 1), with those registered
1184 by the Italian Space Agency-led PRISMA spectrometer (Section 2). While no exact
1185 temporal-spatial coincidence could be achieved, the comparison allowed testing MAJIS
1186 spectral and radiometric response over ocean and clouds, the main targets observed during
1187 this flyby. Clouds observations have been analyzed for the estimation of altitudes and
1188 microphysical properties exploiting different methods (Section 4.2). Ice has been detected in
1189 most of the observations, allowing a first benchmark of the study of its spectral properties
1190 (Section 4.1) in view of Jupiter’s icy satellites’ exploration.

1191 High-altitude emissions from CO_2 and O_3 are also observed in MAJIS dataset, revealing the
1192 presence of a significant number of atmospheric gravity waves, whose properties have been
1193 derived (Section 4.3).

1194 While we discuss *ad hoc* spectral indices for the identification at VIS-NIR wavelengths of
1195 different types of surfaces (in view of the next JUICE Earth flyby happening in September
1196 2026) our investigation of land features is limited to the land/ocean temperature contrast or
1197 to the changing surface altimetry (Section 4.4). Indeed, in the MAJIS 2024 EGA data no land
1198 areas have been captured in daylight.

1199 This wide variety of scientific applications is finally put in the context of the Jupiter case,
1200 taking into account the differences between our planet and the gaseous giant's atmosphere
1201 and icy satellites (Section 5).

1202 In conclusion, EGA data provide the first scientific benchmark of MAJIS instrumental
1203 response in a planetary environment, and give the first glimpse of the amount and quality of
1204 spectral information we can expect in the Jovian system.

1205

1206 **Author Contributions**

1207 Conceptualization, F.O., E.D., A.Mi.; formal analysis, F.O., E.D., A.Mi.; Data Curation, F.O.,
1208 E.D., A.Mi., F.P., Y.L., G.P., A.Z., M.G., E.L., G.S., C.P., S.R., B.S.; investigation, F.O., E.D.,
1209 A.Mi.; methodology, F.O., E.D., A.Mi.; software, F.O., E.D., A.Mi.; supervision, F.O., E.D.,
1210 A.Mi., G.P., F.P., Y.L., G.F., M.C., M.R., B.S., A.M., L.N.F., A.Z., M.G., E.L., G.S., C.P.;
1211 validation, F.O., E.D., A.Mi.; writing—original draft, F.O., E.D., A.Mi.; writing—review &
1212 editing, F.O., E.D., A.Mi., G.P., F.P., L.N.F., A.M.. All authors have read and agreed to this
1213 version of the manuscript.

1214 **Code availability**

1215 The codes used in this manuscript have been developed by the authors and are available on
1216 request.

1217 **Competing interests**

1218 The authors declare no competing interests in the production of this manuscript.

1219

1220 **Acknowledgements & Data availability**

1221

1222 JUICE is a mission under ESA leadership with contributions from its Member States, NASA,
1223 JAXA and the Israel Space Agency. It is the first Large-class mission in ESA's Cosmic Vision
1224 programme. The Italian participation in the JUICE mission is funded by the Italian Space
1225 Agency (ASI). In particular, this work has been developed under the ASI-INAF agreement n.
1226 2023-6-HH.0.

1227 The MAJIS data acquired during the JUICE Moon–Earth flyby in August 2024 are currently
1228 under the mission's cruise-phase proprietary period. These data will be made available
1229 through the ESA Planetary Science Archive following the first Cruise Archive Delivery, which
1230 is currently scheduled for six months after Earth Gravity Assist #3 in 2029.

1231 PRISMA products are generated by IAPS-INAF under a license from ASI Original PRISMA
1232 Product - © Italian Space Agency (ASI) – 2024. ASI retains copyright on the ORIGINAL
1233 Product “PRISMA Product - © Italian Space Agency (ASI) 2024. All rights reserved”.

1234

1235 **References**

1236

1237 Acton, C.H., 1996. Ancillary data services of NASA's navigation and ancillary infor-
1238 mation facility. *Planet. Space Sci.* 44 (1), 65–70.
1239

1240 Acton, C., Bachman, N., Semenov, B., & Wright, E. (2018). A look towards the future
1241 in the handling of space science mission geometry. *Planetary and Space Science*,
1242 150, 9–12. <https://doi.org/10.1016/j.pss.2017.02.013>
1243

1244 Alexander, M. J., and J. R. Holton. "A Model Study of Zonal Forcing in the Equatorial
1245 Stratosphere by Convectively Induced Gravity Waves." *Journal of the Atmospheric*
1246 *Sciences* 54, no. 3 (1997): 408 - 419.
1247 [https://doi.org/10.1175/1520-0469\(1997\)054<0408:amsozf>2.0.co;2](https://doi.org/10.1175/1520-0469(1997)054<0408:amsozf>2.0.co;2).
1248

1249 Alexander, M. Joan, and Christopher Barnet. "Using Satellite Observations to
1250 Constrain Parameterizations of Gravity Wave Effects for Global Models." *Journal of*
1251 *the Atmospheric Sciences* 64, no. 5 (2007): 1652 - 1665.
1252 <https://doi.org/10.1175/jas3897.1>.
1253

1254 Atreya, S.K., M.H. Wong, T.C. Owen, et al. "A Comparison of the Atmospheres of
1255 Jupiter and Saturn: Deep Atmospheric Composition, Cloud Structure, Vertical Mixing,
1256 and Origin." *Planetary and Space Science* 47, nos. 10–11 (1999): 1243 - 1262.
1257 [https://doi.org/10.1016/s0032-0633\(99\)00047-1](https://doi.org/10.1016/s0032-0633(99)00047-1).
1258

1259 Baldridge, A.M., S.J. Hook, C.I. Grove, and G. Rivera. "The ASTER Spectral Library
1260 Version 2.0." *Remote Sensing of Environment* 113, no. 4 (2009): 711 - 715.
1261 <https://doi.org/10.1016/j.rse.2008.11.007>.
1262

1263 Baran, Anthony J. "A Review of the Light Scattering Properties of Cirrus." *Journal of*
1264 *Quantitative Spectroscopy and Radiative Transfer* 110, nos. 14–16 (2009): 1239 -
1265 1260. <https://doi.org/10.1016/j.jqsrt.2009.02.026>.
1266

1267 Bekki, S., and F. Lefevre. "Stratospheric Ozone: History and Concepts and
1268 Interactions with Climate." *The European Physical Journal Conferences* 1 (2009): 113
1269 - 136. <https://doi.org/10.1140/epjconf/e2009-00914-y>.
1270

1271

1272

1273 Biagiotti, F, D Grassi, G Liuzzi, et al. "Evidence of Pure Ammonia Clouds in Jupiter's
1274 Northern Temperate Domain from Juno/JIRAM Infrared Spectral Data." *Monthly*

1275 *Notices of the Royal Astronomical Society* 538, no. 3 (2025): 1535 - 1564.
1276 <https://doi.org/10.1093/mnras/staf381>.

1277

1278 Bjoraker, Gordon L., Michael H. Wong, Imke de Pater, Tilak Hewagama, and Máté
1279 Ádámkóvics. "The Spatial Variation of Water Clouds, NH₃, and H₂O on Jupiter Using
1280 Keck Data at 5 Microns." *Remote Sensing* 14, no. 18 (2022): 4567.
1281 <https://doi.org/10.3390/rs14184567>.

1282

1283 Bockelée-Morvan, D., et al., 2024. Composition and thermal properties of
1284 Ganymede's surface from JWST/NIRSpec and MIRI observations. *A&A*, 681.

1285

1286 Bovensmann, H., J. P. Burrows, M. Buchwitz, et al. "SCIAMACHY: Mission
1287 Objectives and Measurement Modes." *Journal of the Atmospheric Sciences* 56, no. 2
1288 (1999): 127 - 150.
1289 [https://doi.org/10.1175/1520-0469\(1999\)056<0127:smoamm>2.0.co;2](https://doi.org/10.1175/1520-0469(1999)056<0127:smoamm>2.0.co;2).

1290

1291 Butz, A., S. Guerlet, O. Hasekamp, et al. "Toward Accurate CO₂ and CH₄
1292 Observations from GOSAT." *Geophysical Research Letters* 38, no. 14 (2011).
1293 <https://doi.org/10.1029/2011gl047888>.

1294

1295 Cartwright, Richard J., Charles A. Hibbitts, Bryan J. Holler, et al. "Jwst Reveals
1296 Spectral Tracers of Recent Surface Modification on Europa." *The Planetary Science
1297 Journal* 6, no. 5 (2025): 125. <https://doi.org/10.3847/psj/adcab9>.

1298

1299 Cartwright, R.J., et al., 2025. Revealing Callisto's Carbon-rich Surface and CO₂
1300 Atmosphere with JWST. *Planetary Science Journal*, 5, 60.

1301

1302 Cassini, Lorenzo, Guido Masiello, Sergio De Souza-Machado, Manuel
1303 López-Puertas, Larrabee Strow, Giuliano Liuzzi, Christopher Hepplewhite, Tiziano
1304 Maestri, Michele Martinazzo, Carmine Serio, "Updates to 4.3um CO₂ NLTE modeling
1305 for nadir hyperspectral infrared sounders," Proc. SPIE 13668, Remote Sensing of
1306 Clouds and the Atmosphere XXX, 1366809 (29 October 2025);
1307 <https://doi.org/10.1117/12.3069902>

1308

1309 Castagnoli, Chiara, Bianca M. Dinelli, Francesca Altieri, et al. "Characterization and
1310 Sensitivity Analysis of JIRAM Spectra for Optimizing CH₄ and H₃⁺ Retrieval." *The
1311 Planetary Science Journal* 6, no. 4 (2025): 93. <https://doi.org/10.3847/psj/adbf8>.

1312

1313 Clark, Roger N., Dale P. Cruikshank, Ralf Jaumann, et al. "The Surface Composition
1314 of Iapetus: Mapping Results from Cassini VIMS." *Icarus* 218, no. 2 (2012): 831 - 860.
1315 <https://doi.org/10.1016/j.icarus.2012.01.008>.

1316

1317 Coradini, A., F. Capaccioni, P. Drossart, A. Semery, G. Arnold, and U. Schade.
1318 "VIRTIS: The Imaging Spectrometer of the Rosetta Mission." *Advances in Space*
1319 *Research* 24, no. 9 (1999): 1095 - 1104.
1320 [https://doi.org/10.1016/s0273-1177\(99\)80203-8](https://doi.org/10.1016/s0273-1177(99)80203-8).

1321

1322 Cox, C., and Munk, W., "Measurement of the Roughness of the Sea Surface from
1323 Photographs of the Sun's Glitter," *J. Opt. Soc. Am.* **44**, 838-850 (1954)
1324 <https://doi.org/10.1364/JOSA.44.000838>

1325

1326 D'Aversa, Emiliano, Fabrizio Oliva, Francesca Altieri, et al. "Vertical Distribution of
1327 Dust in the Martian Atmosphere: OMEGA/MEx Limb Observations." *Icarus* 371
1328 (January 2022): 114702. <https://doi.org/10.1016/j.icarus.2021.114702>.

1329

1330 D'Aversa, E., et al.: Spectroscopic detection of terrestrial lightning from space by
1331 JUICE-MAJIS during Earth Gravity Assist, *Ann. Geophys.*, submitted to this issue.

1332

1333 Dewan, E. M., and R. E. Good. "Saturation and the 'Universal' Spectrum for Vertical
1334 Profiles of Horizontal Scalar Winds in the Atmosphere." *Journal of Geophysical*
1335 *Research: Atmospheres* 91, no. D2 (1986): 2742 - 2748.
1336 <https://doi.org/10.1029/jd091id02p02742>.

1337

1338 Dewan, E. M., R. H. Picard, R. R. O'Neil, et al. "MSX Satellite Observations of
1339 Thunderstorm-generated Gravity Waves in Mid-wave Infrared Images of the Upper
1340 Stratosphere." *Geophysical Research Letters* 25, no. 7 (1998): 939 - 942.
1341 <https://doi.org/10.1029/98gl00640>.

1342

1343 Dolan, Brenda, Pavlos Kollias, Susan C. van den Heever, et al. "Time Resolved
1344 Reflectivity Measurements of Convective Clouds." *Geophysical Research Letters* 50,
1345 no. 22 (2023). <https://doi.org/10.1029/2023gl105723>.

1346

1347 Dörnbrack, Andreas, Thomas Birner, Andreas Fix, et al. "Evidence for Inertia Gravity

1348 Waves Forming Polar Stratospheric Clouds over Scandinavia.” *Journal of*
1349 *Geophysical Research: Atmospheres* 107, no. D20 (2002).
1350 <https://doi.org/10.1029/2001jd000452>.
1351
1352 Drossart, Pierre, Giuseppe Piccioni, Angioletta Coradini, et al. “VIRTIS Imaging
1353 Spectrometer for the ESA/Venus Express Mission.” *SPIE Proceedings* 5543
1354 (November 2004): 175. <https://doi.org/10.1117/12.557427>.
1355
1356 Eckermann, Stephen D., Jun Ma, Dong L. Wu, and Dave Broutman. “A
1357 Three-dimensional Mountain Wave Imaged in Satellite Radiance throughout the
1358 Stratosphere: Evidence of the Effects of Directional Wind Shear.” *Quarterly Journal of*
1359 *the Royal Meteorological Society* 133, no. 629 (2007): 1959 - 1975.
1360 <https://doi.org/10.1002/qj.187>.
1361
1362 Efremenko, Dmitry, and Alexander Kokhanovsky. *Foundations of Atmospheric*
1363 *Remote Sensing*. Springer Nature, 2021.
1364
1365 Ehrlich, A., E. Bierwirth, M. Wendisch, et al. “Cloud Phase Identification of Arctic
1366 Boundary-Layer Clouds from Airborne Spectral Reflection Measurements: Test of
1367 Three Approaches.” *Atmospheric Chemistry and Physics* 8, no. 24 (2008): 7493 -
1368 7505. <https://doi.org/10.5194/acp-8-7493-2008>.
1369
1370 Eldering, Annmarie, Thomas E. Taylor, Christopher W. O’Dell, and Ryan Pavlick.
1371 “The OCO-3 Mission: Measurement Objectives and Expected Performance Based on
1372 1 Year of Simulated Data.” *Atmospheric Measurement Techniques* 12, no. 4 (2019):
1373 2341 - 2370. <https://doi.org/10.5194/amt-12-2341-2019>.
1374
1375 Filacchione, Gianrico, Emiliano D’Aversa, Fabrizio Capaccioni, et al. “Saturn’s Icy
1376 Satellites Investigated by Cassini-VIMS. IV. Daytime Temperature Maps.” *Icarus* 271
1377 (June 2016): 292 - 313. <https://doi.org/10.1016/j.icarus.2016.02.019>.
1378
1379 Filacchione, G., Capaccioni, F., Ciarniello, M., et al., 2012. Saturn’s icy satellites and
1380 rings investigated by cassini-VIMS: III—Radial compositional variability. *Icarus*
1381 220, 1064–1096.
1382
1383 Fink, Uwe, and Harold P. Larson. “Temperature Dependence of the Water-Ice
1384 Spectrum between 1 and 4 Microns: Application to Europa, Ganymede and Saturn’s

1385 Rings." *Icarus* 24, no. 4 (1975): 411 - 420.
1386 [https://doi.org/10.1016/0019-1035\(75\)90058-5](https://doi.org/10.1016/0019-1035(75)90058-5).

1387
1388 Fletcher, L.N., et al., 2023. Jupiter Science Enabled by ESA's Jupiter Icy Moons
1389 Explorer. *Space Science Review*, vol. 219, n. 53, 2023.

1390
1391 Fovell, R., D. Durran, and J. R. Holton. "Numerical Simulations of Convectively
1392 Generated Stratospheric Gravity Waves." *Journal of the Atmospheric Sciences* 49,
1393 no. 16 (1992): 1427 - 1442.
1394 [https://doi.org/10.1175/1520-0469\(1992\)049<1427:nsocgs>2.0.co;2](https://doi.org/10.1175/1520-0469(1992)049<1427:nsocgs>2.0.co;2).

1395
1396 Fritts, David C., and M. Joan Alexander. "Gravity Wave Dynamics and Effects in the
1397 Middle Atmosphere." *Reviews of Geophysics* 41, no. 1 (2003).
1398 <https://doi.org/10.1029/2001rg000106>.

1399
1400 Fu, Dongwei, Larry Di Girolamo, Robert M. Rauber, et al. "An Evaluation of the Liquid
1401 Cloud Droplet Effective Radius Derived from MODIS, Airborne Remote Sensing, and
1402 in Situ Measurements from CAMP2Ex." *Atmospheric Chemistry and Physics* 22, no.
1403 12 (2022): 8259 - 8285. <https://doi.org/10.5194/acp-22-8259-2022>.

1404
1405 Geddes, A., and H. Bösch. "Tropospheric Aerosol Profile Information from
1406 High-Resolution Oxygen A-Band Measurements from Space." *Atmospheric
1407 Measurement Techniques* 8, no. 2 (2015): 859 - 874.
1408 <https://doi.org/10.5194/amt-8-859-2015>.

1409
1410 Gordon, I.E., L.S. Rothman, R.J. Hargreaves, et al. "The HITRAN2020 Molecular
1411 Spectroscopic Database." *Journal of Quantitative Spectroscopy and Radiative
1412 Transfer* 277 (January 2022): 107949. <https://doi.org/10.1016/j.jqsrt.2021.107949>.

1413
1414 Gorshchev, V., A. Serdyuchenko, M. Weber, W. Chehade, and J. P. Burrows. "High
1415 Spectral Resolution Ozone Absorption Cross-Sections – Part 1: Measurements, Data
1416 Analysis and Comparison with Previous Measurements around 293 K." *Atmospheric
1417 Measurement Techniques* 7, no. 2 (2014): 609 - 624.
1418 <https://doi.org/10.5194/amt-7-609-2014>.

1419
1420
1421

1422 Grassi, Davide, A Mura, G Sindoni, et al. "On the Clouds and Ammonia in Jupiter's
1423 Upper Troposphere from Juno JIRAM Reflectivity Observations." *Monthly Notices of*
1424 *the Royal Astronomical Society* 503, no. 4 (2021): 4892 - 4907.
1425 <https://doi.org/10.1093/mnras/stab740>.
1426

1427 Grassi, D., et al., 2020. On the Spatial Distribution of Minor Species in Jupiter's
1428 Troposphere as Inferred From Juno JIRAM Data. *JGR Planets*, 125, 4.
1429

1430 Greeley, R., C.F. Chyba, J.W. Head III, W.B. McKinnon, R.T. Pappalardo, and P.H.
1431 Figueredo. "The Geology of Europa." In *Jupiter: The Planet, Satellites and*
1432 *Magnetosphere*, edited by F. Bagenal, T. Dowling, and W. McKinnon. Cambridge
1433 University Press, 2007.
1434

1435 Grundy, W. M., and B. Schmitt. "The Temperature-dependent Near-infrared
1436 Absorption Spectrum of Hexagonal H₂O Ice." *Journal of Geophysical Research:*
1437 *Planets* 103, no. E11 (1998): 25809 - 25822. <https://doi.org/10.1029/98je00738>.
1438
1439

1440 Guerlet, S., Lauzanne, N., Armante, R., Poulet, F., and Langevin, Y.: MAJIS/JUICE
1441 performances in the infrared during Earth fly-by: comparisons with IASI
1442 measurements and sensitivity to trace species, *Ann. Geophys.*, submitted to this
1443 issue.
1444

1445

1446 Haffoud, Paolo, François Poulet, Mathieu Vincendon, et al. "Calibration of MAJIS
1447 (Moons And Jupiter Imaging Spectrometer). III. Spectral Calibration." *Review of*
1448 *Scientific Instruments* 95, no. 3 (2024). <https://doi.org/10.1063/5.0188944>.
1449

1450 Hale, George M., and Marvin R. Querry. "Optical Constants of Water in the 200 Nm to
1451 200 Mm Wavelength Region." *Applied Optics* 12, no. 3 (1973): 555.
1452 <https://doi.org/10.1364/ao.12.000555>.
1453

1454 Hamilton, Kevin. "Comprehensive Meteorological Modelling of the Middle
1455 Atmosphere: A Tutorial Review." *Journal of Atmospheric and Terrestrial Physics* 58,
1456 no. 14 (1996): 1591 - 1627. [https://doi.org/10.1016/0021-9169\(96\)00028-1](https://doi.org/10.1016/0021-9169(96)00028-1).
1457

1458 Heintzenberg, J., D. C. Covert, and R. Van Dingenen. "Size Distribution and
1459 Chemical Composition of Marine Aerosols: A Compilation and Review." *Tellus B:
1460 Chemical and Physical Meteorology* 52, no. 4 (2000): 1104.
1461 <https://doi.org/10.3402/tellusb.v52i4.17090>.

1462

1463 Hines, C. O. "Internal Atmospheric Gravity Waves at Ionospheric Heights." *Canadian
1464 Journal of Physics* 38, no. 11 (1960): 1441 - 1481. <https://doi.org/10.1139/p60-150>.

1465

1466 Hueso, R., A. Sánchez-Lavega, G. Piccioni, et al. "Morphology and Dynamics of
1467 Venus Oxygen Airglow from Venus Express/Visible and Infrared Thermal Imaging
1468 Spectrometer Observations." *Journal of Geophysical Research: Planets* 113, no. E5
1469 (2008). <https://doi.org/10.1029/2008je003081>.

1470

1471 Hueso, R., et al., JUICE-JANUS observations of Earth in preparation for the JANUS
1472 investigation of Jupiter's atmosphere. *Ann. Geophys.*, submitted to this issue.

1473

1474

1475 Hurley, J., P.G.J. Irwin, A. Adriani, et al. "Analysis of Rosetta/VIRTIS Spectra of Earth
1476 Using Observations from ENVISAT/AATSR, TERRA/MODIS and
1477 ENVISAT/SCIAMACHY, and Radiative-Transfer Simulations." *Planetary and Space
1478 Science* 90 (January 2014): 37 - 59. <https://doi.org/10.1016/j.pss.2013.06.012>.

1479

1480 Kim, Young-Joon, Stephen D. Eckermann, and Hye-Yeong Chun. "An Overview of
1481 the Past, Present and Future of Gravity-wave Drag Parametrization for Numerical
1482 Climate and Weather Prediction Models." *Atmosphere-Ocean* 41, no. 1 (2003): 65 -
1483 98. <https://doi.org/10.3137/ao.410105>.

1484

1485 Kitamura, Rei, Laurent Pilon, and Mirosław Jonasz. "Optical Constants of Silica Glass
1486 from Extreme Ultraviolet to Far Infrared at near Room Temperature." *Applied Optics*
1487 46, no. 33 (2007): 8118. <https://doi.org/10.1364/ao.46.008118>.

1488

1489 Krisna, Trismono C., Manfred Wendisch, André Ehrlich, et al. "Comparing Airborne
1490 and Satellite Retrievals of Cloud Optical Thickness and Particle Effective Radius
1491 Using a Spectral Radiance Ratio Technique: Two Case Studies for Cirrus and Deep
1492 Convective Clouds." *Atmospheric Chemistry and Physics* 18, no. 7 (2018): 4439 -
1493 4462. <https://doi.org/10.5194/acp-18-4439-2018>.

1494

1495 Kuang, Zhiming, Jack Margolis, Geoffrey Toon, David Crisp, and Yuk Yung.
1496 “Spaceborne Measurements of Atmospheric CO₂ by High-resolution NIR
1497 Spectrometry of Reflected Sunlight: An Introductory Study.” *Geophysical Research*
1498 *Letters* 29, no. 15 (2002). <https://doi.org/10.1029/2001gl014298>.
1499

1500 Kurucz, R.L., (1995), The solar irradiance by computation, Proc 17th Annual
1501 Conference Transmission Models, Phillips Laboratory, Hanscom AFB,
1502 PL-TR-95-2060. G.P. Anderson, et al. Eds. PP 333-334.
1503

1504 Kurucz, R.L., et al. (1984), Solar Flux atlas from 296 to 1300 nm, National Solar
1505 Observatory Atlas No. 1. NOAO, Sunspot, NM.
1506

1507 Khurana, K.K., et al., 2007. The origin of Ganymedes’ polar caps. *Icarus*, 191, 1,
1508 193-202. <https://doi.org/10.1016/j.icarus.2007.04.022>
1509

1510 Langevin, Y., F. Poulet, G. Piccioni, et al. “Calibration of MAJIS (Moons and Jupiter
1511 Imaging Spectrometer). IV. Radiometric Calibration (Invited).” *Review of Scientific*
1512 *Instruments* 95, no. 11 (2024). <https://doi.org/10.1063/5.0202702>.
1513

1514 Langevin, Y., Rodriguez, S., Poulet, F., Guerlet, S., Armante, R., Agostini, L.,
1515 D’Aversa, E., Royer, C., Fletcher, L., Oliva, F., Seignovert, B., Stephan, K., and Tosi,
1516 F.: Post-launch spectral and radiometric performances of MAJIS, the VIS–NIR
1517 imaging spectrometer of JUICE, *Ann. Geophys.*, submitted to this issue.

1518

1519 LeMone, Margaret A. “International Cloud Atlas: Manual on the Observation of
1520 Clouds and Other Meteors.” In *International Cloud Atlas*. World Meteorological
1521 Organization, 1988.
1522

1523 Ligier, N., C. Paranicas, J. Carter, et al. “Surface Composition and Properties of
1524 Ganymede: Updates from Ground-Based Observations with the near-Infrared
1525 Imaging Spectrometer SINFONI/VLT/ESO.” *Icarus* 333 (November 2019): 496 - 515.
1526 <https://doi.org/10.1016/j.icarus.2019.06.013>.
1527

1528 *Lopinto, E., Fasano, L., Longo, F., Varacalli, G., Sacco, P., Chiarantini, L., Sarti, F.,*
1529 *Agrimano, L., Santoro, F., Cogliati, S., Colombo, R., Bresciani, M., Giardino, C.,*
1530 *Braga, F. (2021). Current Status and Future Perspectives of the PRISMA Mission at*

1531 the Turn of One Year in Operational Usage 2021 IEEE International Geoscience and
1532 Remote Sensing Symposium IGARSS
1533 <https://doi.org/10.1109/IGARSS47720.2021.9553301>

1534

1535 Luo, Tao, Renmin Yuan, and Zhien Wang. "On Factors Controlling Marine Boundary
1536 Layer Aerosol Optical Depth." *Journal of Geophysical Research: Atmospheres* 119,
1537 no. 6 (2014): 3321 - 3334. <https://doi.org/10.1002/2013jd020936>.

1538

1539 Mastrapa, R, M Bernstein, S Sandford, T Roush, D Cruikshank, and C Ore. "Optical
1540 Constants of Amorphous and Crystalline H₂O Ice in the near Infrared from 1.1 to 2.6
1541 μm ." *Icarus* 197, no. 1 (2008): 307 - 320.
1542 <https://doi.org/10.1016/j.icarus.2008.04.008>.

1543

1544 Mastrapa, R. M., S. A. Sandford, T. L. Roush, D. P. Cruikshank, and C. M. Dalle Ore.
1545 "Optical Constant of Amorphous and Crystalline H₂O Ice: 2.5-22 Mm (4000-455
1546 Cm⁻¹) Optical Constants of H₂O Ice." *The Astrophysical Journal* 701, no. 2 (2009):
1547 1347 - 1356. <https://doi.org/10.1088/0004-637x/701/2/1347>.

1548

1549 Melin, H., O'Donoghue, J., Moore, L., Stallard, T. S., Fletcher, L. N., Roman, M. T.,
1550 Harkett, J., King, O. R. T., Thomas, E. M., Wang, R., Tiranti, P. I., Knowles, K. L., de
1551 Pater, I., Fouchet, T., Fry, P. H., Wong, M. H., Holler, B. J., Hueso, R., James, M. K.,
1552 ... Showalter, M. R. (2024). Ionospheric irregularities at Jupiter observed by JWST.
1553 *Nature Astronomy*, 8(8), 1000–1007. <https://doi.org/10.1038/s41550-024-02305-9>.

1554

1555 Migliorini, A., B. M. Dinelli, C. Castagnoli, et al. "First Observations of CH₄ and
1556 Spatially Resolved Emission Layers at Jupiter Equator, as Seen by JIRAM/Juno."
1557 *Journal of Geophysical Research: Planets* 128, no. 3 (2023).
1558 <https://doi.org/10.1029/2022je007509>.

1559

1560 Miller, Steve, Jonathan Tennyson, Thomas R. Geballe, and Tom Stallard. "Thirty
1561 Years of H₃⁺ Astronomy." *Reviews of Modern Physics* 92, no. 3 (2020).
1562 <https://doi.org/10.1103/revmodphys.92.035003>.

1563

1564 Moriconi, M. L., A. Migliorini, F. Altieri, et al. "Turbulence Power Spectra in Regions

1565 Surrounding Jupiter's South Polar Cyclones from Juno/JIRAM." *Journal of*
1566 *Geophysical Research: Planets* 125, no. 7 (2020).
1567 <https://doi.org/10.1029/2019je006096>.
1568
1569 Müller-Wodarg, I. C. F., T. T. Koskinen, L. Moore, et al. "Atmospheric Waves and
1570 Their Possible Effect on the Thermal Structure of Saturn's Thermosphere."
1571 *Geophysical Research Letters* 46, no. 5 (2019): 2372 - 2380.
1572 <https://doi.org/10.1029/2018gl081124>.
1573
1574 Nakajima, Takashi Y., Haruma Ishida, Takashi M. Nagao, et al. "Theoretical Basis of
1575 the Algorithms and Early Phase Results of the GCOM-C (Shikisai) SGLI Cloud
1576 Products." *Progress in Earth and Planetary Science* 6, no. 1 (2019).
1577 <https://doi.org/10.1186/s40645-019-0295-9>.
1578
1579 Nastrom, Gregory D., and David C. Fritts. "Sources of Mesoscale Variability of
1580 Gravity Waves. Part i: Topographic Excitation." *Journal of the Atmospheric Sciences*
1581 49, no. 2 (1992): 101 - 110.
1582 [https://doi.org/10.1175/1520-0469\(1992\)049<0101:somvog>2.0.co;2](https://doi.org/10.1175/1520-0469(1992)049<0101:somvog>2.0.co;2).
1583
1584 Newnham, David A., and John Ballard. "Visible Absorption Cross Sections and
1585 Integrated Absorption Intensities of Molecular Oxygen (O₂ and O₄)." *Journal of*
1586 *Geophysical Research: Atmospheres* 103, no. D22 (1998): 28801 - 28815.
1587 <https://doi.org/10.1029/98jd02799>.
1588
1589 O'Donoghue, J., L. Moore, T. S. Stallard, and H. Melin. "Heating of Jupiter's Upper
1590 Atmosphere above the Great Red Spot." *Nature* 536, no. 7615 (2016): 190 - 192.
1591 <https://doi.org/10.1038/nature18940>.
1592
1593 Oliva, F., A. Adriani, M.L. Moriconi, G.L. Liberti, E. D'Aversa, and G. Filacchione.
1594 "Clouds and Hazes Vertical Structure of a Saturn's Giant Vortex from Cassini/VIMS-V
1595 Data Analysis." *Icarus* 278 (November 2016): 215 - 237.
1596 <https://doi.org/10.1016/j.icarus.2016.06.021>.
1597
1598 Oliva, F., A. Geminale, E. D'Aversa, et al. "Properties of a Martian Local Dust Storm
1599 in Atlantis Chaos from OMEGA/MEX Data." *Icarus* 300 (January 2018): 1 - 11.
1600 <https://doi.org/10.1016/j.icarus.2017.07.034>.
1601

1602 Oliva, F., G. Piccioni, E. D'Aversa, et al. "Earth as an Exoplanet: VIRTIS-M/Venus
1603 Express Data Analysis." *EPSC Abstracts* 11 (2017).
1604

1605 Orton, G.S., et al., 2017. The first close-up images of Jupiter's polar regions: Results
1606 from the Juno mission JunoCam instrument. *Geophysical Research Letters*, 44, 10,
1607 4599-4606.
1608

1609 Peralta, J., R. Hueso, A. Sánchez-Lavega, G. Piccioni, O. Lanciano, and P. Drossart.
1610 "Characterization of Mesoscale Gravity Waves in the Upper and Lower Clouds of
1611 Venus from VEX-VIRTIS Images." *Journal of Geophysical Research: Planets* 113, no.
1612 E5 (2008). <https://doi.org/10.1029/2008je003185>.
1613

1614 Piani, C., D. Durran, M. J. Alexander, and J. R. Holton. "A Numerical Study of
1615 Three-Dimensional Gravity Waves Triggered by Deep Tropical Convection and Their
1616 Role in the Dynamics of the QBO." *Journal of the Atmospheric Sciences* 57, no. 22
1617 (2000): 3689 - 3702.
1618 [https://doi.org/10.1175/1520-0469\(2000\)057<3689:ansotd>2.0.co;2](https://doi.org/10.1175/1520-0469(2000)057<3689:ansotd>2.0.co;2).
1619

1620 Piccioni, Giuseppe, Alessandro Bini, Giulio Bugetti, et al. "Scientific Goals and
1621 Technical Challenges of the MAJIS Imaging Spectrometer for the JUICE Mission."
1622 *2019 IEEE 5th International Workshop on Metrology for AeroSpace*
1623 *(MetroAeroSpace)*, IEEE, June 2019, 318 - 323.
1624 <https://doi.org/10.1109/metroaerospace.2019.8869566>.
1625

1626 S. Pignatti *et al.*, "The PRISMA hyperspectral mission: Science activities and
1627 opportunities for agriculture and land monitoring," *2013 IEEE International*
1628 *Geoscience and Remote Sensing Symposium - IGARSS*, Melbourne, VIC, Australia,
1629 2013, pp. 4558-4561, doi: 10.1109/IGARSS.2013.6723850.
1630

1631 Poulet, F., G. Piccioni, Y. Langevin, et al. "Moons and Jupiter Imaging Spectrometer
1632 (MAJIS) on Jupiter Icy Moons Explorer (JUICE)." *Space Science Reviews* 220, no. 3
1633 (2024a). <https://doi.org/10.1007/s11214-024-01057-2>.
1634

1635 Poulet, F., Piccioni, G., Langevin, Y., et al. ESA/JUICE encounters Earth/Moon in
1636 2024: overview of the Moons And Jupiter Imaging Spectrometer (MAJIS)
1637 observations. *Ann. Geophys.*, submitted to this issue
1638

1639 Poulet, F., Langevin, Y., and Piccioni, G.: Calibration of the Moons And Jupiter
1640 Imaging Spectrometer (MAJIS): Introduction to the special collection and summary of
1641 the performances, *Rev. Sci. Instrum.*, 95, 071601, <https://doi.org/10.1063/5.0209679>,
1642 2024b

1643

1644 Rossow, William B., and Robert A. Schiffer. "Advances in Understanding Clouds from
1645 ISCCP." *Bulletin of the American Meteorological Society* 80, no. 11 (1999): 2261 -
1646 2287. [https://doi.org/10.1175/1520-0477\(1999\)080<2261:aiucfi>2.0.co;2](https://doi.org/10.1175/1520-0477(1999)080<2261:aiucfi>2.0.co;2).

1647

1648 Seignovert, B., Poulet, F., Langevin, Y., D'Aversa, E., Ligier, N., Mesbout, M., Leyrat,
1649 C., Le Mouélic, S., Stephan, K., Palumbo, P., Agostini, L., Pensa, L., Le Deit, L.,
1650 Cornet, T., Belgacem, I., Costa, M., and Escalante Lopez, A.: MAJIS onboard
1651 geometric calibration during 1320 the early cruise phase, *Ann. Geophys.*, submitted
1652 to this issue.

1653

1654 Serdyuchenko, A., Gorshchev, V., Weber, M., Chehade, W., and Burrows, J. P.: High
1655 spectral resolution ozone absorption cross-sections – Part 2: Temperature
1656 dependence, *Atmos. Meas. Tech.*, 7, 625–636,
1657 <https://doi.org/10.5194/amt-7-625-2014>, 2014.

1658

1659 Simon, A. A., L. Li, and D. C. Reuter. "Small-scale Waves on Jupiter: A Reanalysis of
1660 New Horizons, Voyager, and Galileo Data." *Geophysical Research Letters* 42, no. 8
1661 (2015): 2612 - 2618. <https://doi.org/10.1002/2015gl063433>.

1662

1663 Sindoni, G., D. Grassi, A. Adriani, et al. "Characterization of the White Ovals on
1664 Jupiter's Southern Hemisphere Using the First Data by the Juno/JIRAM Instrument."
1665 *Geophysical Research Letters* 44, no. 10 (2017): 4660 - 4668.
1666 <https://doi.org/10.1002/2017gl072940>.

1667

1668 Smirnov, Alexander, Brent N. Holben, Yoram J. Kaufman, et al. "Optical Properties of
1669 Atmospheric Aerosol in Maritime Environments." *Journal of the Atmospheric*
1670 *Sciences* 59, no. 3 (2002): 501 - 523.
1671 [https://doi.org/10.1175/1520-0469\(2002\)059<0501:opoaai>2.0.co;2](https://doi.org/10.1175/1520-0469(2002)059<0501:opoaai>2.0.co;2).

1672

1673 Smith, K.M, and D.A Newnham. "Near-Infrared Absorption Spectroscopy of Oxygen
1674 and Nitrogen Gas Mixtures." *Chemical Physics Letters* 308, nos. 1–2 (1999): 1 - 6.
1675 [https://doi.org/10.1016/s0009-2614\(99\)00584-9](https://doi.org/10.1016/s0009-2614(99)00584-9).

1676
1677 Stephan, Katrin, Mauro Ciarniello, Olivier Poch, Bernard Schmitt, David Haack, and
1678 Andrea Raponi. "VIS-NIR/SWIR Spectral Properties of H₂O Ice Depending on
1679 Particle Size and Surface Temperature." *Minerals* 11, no. 12 (2021): 1328.
1680 <https://doi.org/10.3390/min11121328>.
1681
1682 Stephan, Katrin, T. Roatsch, F. Tosi, et al. "Regions of Interest on Ganymede's and
1683 Callisto's Surfaces as Potential Targets for ESA's JUICE Mission." *Planetary and
1684 Space Science* 208 (November 2021a): 105324.
1685 <https://doi.org/10.1016/j.pss.2021.105324>.
1686
1687 Stevens, Michael H., Christoph R. Englert, John M. Harlander, et al. "Retrieval of
1688 Lower Thermospheric Temperatures from O₂ A Band Emission: The MIGHTI
1689 Experiment on ICON." *Space Science Reviews* 214, no. 1 (2017).
1690 <https://doi.org/10.1007/s11214-017-0434-9>.
1691
1692 Sun, Kangwen, Guangyao Dai, Songhua Wu, et al. *Correlation between Marine
1693 Aerosol Optical Properties and Wind Fields over Remote Oceans with Use of
1694 Spaceborne Lidar Observations*. Copernicus GmbH, 2023.
1695 <https://doi.org/10.5194/egusphere-2023-433>.
1696
1697 Taylor, M.J., and M.A. Hapgood. "Identification of a Thunderstorm as a Source of
1698 Short Period Gravity Waves in the Upper Atmospheric Nightglow Emissions."
1699 *Planetary and Space Science* 36, no. 10 (1988): 975 - 985.
1700 [https://doi.org/10.1016/0032-0633\(88\)90035-9](https://doi.org/10.1016/0032-0633(88)90035-9).
1701
1702 Thomason, L. W., S. P. Burton, B.-P. Luo, and T. Peter. "SAGE II Measurements of
1703 Stratospheric Aerosol Properties at Non-Volcanic Levels." *Atmospheric Chemistry
1704 and Physics* 8, no. 4 (2008): 983 - 995. <https://doi.org/10.5194/acp-8-983-2008>.
1705
1706 Tosi, Federico, Thomas Roatsch, André Galli, et al. "Characterization of the Surfaces
1707 and Near-Surface Atmospheres of Ganymede, Europa and Callisto by JUICE."
1708 *Space Science Reviews* 220, no. 5 (2024).
1709 <https://doi.org/10.1007/s11214-024-01089-8>.
1710
1711 van Diedenhoven, Bastiaan, Ann M. Fridlind, Brian Cairns, Andrew S. Ackerman, and
1712 John E. Yorks. "Vertical Variation of Ice Particle Size in Convective Cloud Tops."

1713 *Geophysical Research Letters* 43, no. 9 (2016): 4586 - 4593.
1714 <https://doi.org/10.1002/2016gl068548>.

1715

1716 Veefkind, J.P., I. Aben, K. McMullan, et al. "TROPOMI on the ESA Sentinel-5
1717 Precursor: A GMES Mission for Global Observations of the Atmospheric Composition
1718 for Climate, Air Quality and Ozone Layer Applications." *Remote Sensing of
1719 Environment* 120 (May 2012): 70 - 83. <https://doi.org/10.1016/j.rse.2011.09.027>.

1720

1721 Voudouri, Kalliopi Artemis, Konstantinos Michailidis, Maria-Elissavet Koukouli, et al.
1722 "Investigating a Persistent Stratospheric Aerosol Layer Observed over Southern
1723 Europe during 2019." *Remote Sensing* 15, no. 22 (2023): 5394.
1724 <https://doi.org/10.3390/rs15225394>.

1725

1726 Warren, Stephen G., and Richard E. Brandt. "Optical Constants of Ice from the
1727 Ultraviolet to the Microwave: A Revised Compilation." *Journal of Geophysical
1728 Research: Atmospheres* 113, no. D14 (2008). <https://doi.org/10.1029/2007jd009744>.

1729

1730 Wei, Lesi, Huazhe Shang, Jian Xu, et al. "Cloud Top Pressure Retrieval Using
1731 Polarized and Oxygen A-Band Measurements from GF5 and PARASOL Satellites."
1732 *Advances in Atmospheric Sciences* 41, no. 4 (2024): 680 - 700.
1733 <https://doi.org/10.1007/s00376-023-2382-5>.

1734

1735 Zheng, Guangjie, Yang Wang, Allison C. Aiken, et al. "Marine Boundary Layer
1736 Aerosol in the Eastern North Atlantic: Seasonal Variations and Key Controlling
1737 Processes." *Atmospheric Chemistry and Physics* 18, no. 23 (2018): 17615 - 17635.
1738 <https://doi.org/10.5194/acp-18-17615-2018>.

1739

1740 Zhou, Yongbo, Xuejin Sun, Tero Mielonen, et al. "Cirrus Cloud Optical Thickness and
1741 Effective Diameter Retrieved by MODIS: Impacts of Single Habit Assumption, 3-d
1742 Radiative Effects, and Cloud Inhomogeneity." *Journal of Geophysical Research:
1743 Atmospheres* 123, no. 2 (2018): 1195 - 1210. <https://doi.org/10.1002/2017jd027232>.

1744

1745 Zinner, T., Hausmann, P., Ewald, F., Bugliaro, L., Emde, C., Mayer, B.,
1746 "Ground-based imaging remote sensing of ice clouds: uncertainties caused by
1747 sensor, method and atmosphere." *Atmospheric Measurements Techniques*, Volume
1748 9, issue 9, 4615–4632, (2016) <https://doi.org/10.5194/amt-9-4615-2016>

1749